

Dart-Leader and K-Leader Velocity From Initiation Site to Termination Time-Resolved with 3D Interferometry

Daniel Jensen^{1,1}, Richard G. Sonnenfeld^{2,2}, Mark A. Stanley^{3,3}, Harald E. Edens^{1,1},
Caitano L. da Silva^{4,4}, and Paul R. Krehbiel^{2,2}

¹New Mexico Institute of Mining and Technology

²New Mexico Tech

³LANL

⁴New Mexico Institute of Mining & Technology

November 30, 2022

Abstract

Simultaneous data from two interferometers separated by 16 km and synchronized within 100 ns was collected for a thunderstorm near Langmuir Lab on October 23, 2018. Analysis via triangulation followed by a least-squares fit to time of arrival across all six antennae produced a three-dimensional interferometer data set (3DINTF). Simultaneous Lightning Mapping Array (LMA) data enabled an independent calculation of 3DINTF accuracy, yielding a median location uncertainty of 200 m. This is the most accurate verified result to date for a two-station interferometer. The 3D data allowed profiling the velocity of multiple dart leaders and K leaders that followed the same channel. 3D velocities calculated from the in-cloud initiation site to ground ranged from 3×10^6 m/s to 20×10^6 m/s. Average velocity generally increased with subsequent leaders, consistent with increased conditioning of the channel. Also, all leaders showed a factor of two to three decrease in velocity as they proceeded over 15 km of channel. We speculate that the velocity decrease is consistent with energy lost in the reionization of the channel at the leader tip. This paper includes an appendix providing details of the triangulation technique used.

1 **Dart-Leader and K-Leader Velocity From Initiation**
2 **Site to Termination Time-Resolved with 3D**
3 **Interferometry**

4 **Daniel P. Jensen, Richard G. Sonnenfeld, Mark A. Stanley, Harald E. Edens,**
5 **Caitano L. da Silva, Paul R. Krehbiel**

6 Langmuir Laboratory for Atmospheric Research, at New Mexico Institute of Mining and Technology

7 **Key Points:**

- 8 • Two K leaders and three dart leaders were recorded on the same channel for one
9 flash using a 3D Interferometer (3DINTF).
10 • Average velocity generally increased with successive leaders on the same channel.
11 • Dart leader and K leader velocity consistently decreased with progress along the
12 channel for the analyzed flash.

Corresponding author: Daniel Jensen, djensen@alumni.nmt.edu

Abstract

Simultaneous data from two interferometers separated by 16 km and synchronized within 100 ns was collected for a thunderstorm near Langmuir Lab on October 23, 2018. Analysis via triangulation followed by a least-squares fit to time of arrival across all six antennae produced a three-dimensional interferometer data set (3DINTF). Simultaneous Lightning Mapping Array (LMA) data enabled an independent calculation of 3DINTF accuracy, yielding a median location uncertainty of 200 m. This is the most accurate verified result to date for a two-station interferometer. The 3D data allowed profiling the velocity of multiple dart leaders and K leaders that followed the same channel. 3D velocities calculated from the in-cloud initiation site to ground ranged from 3×10^6 m/s to 20×10^6 m/s. Average velocity generally increased with subsequent leaders, consistent with increased conditioning of the channel. Also, all leaders showed a factor of two to three decrease in velocity as they proceeded over 15 km of channel. We speculate that the velocity decrease is consistent with energy lost in the reionization of the channel at the leader tip. This paper includes an appendix providing details of the triangulation technique used.

1 Introduction**1.1 Brief History of VHF Instrumentation for Lightning Studies**

Very High Frequency (VHF) radiation has been used to study lightning since the 1960's because of its ability to penetrate clouds, where most lightning activity occurs. This type of instrument was pioneered by Oetzel and Pierce (1969), who describe an instrument with three antennas ~ 30 m apart arranged in a right triangle. Their design was narrowband but they suggested signal strengths should be sufficient for any band between 30 MHz and 100 MHz. This design bore a striking resemblance to modern interferometers (INTF), but it only measured the azimuthal direction to a flash. The early INTFs of Warwick et al. (1979), Hayenga (1984) and, Rhodes et al. (1994) used analog phase detection (mixers) due to limitations in digital technology. They operated in narrow frequency bands so that the intermediate frequency signal was within band of available signal processing electronics. These INTFs could measure both the azimuth and elevation of sources, but not the range to the source. Narrow-band INTFs can improve their angular resolution by adding antennas on baselines of different lengths to allow the elimination of phase ambiguity (Rhodes et al., 1994; Shao & Krehbiel, 1996).

Beginning in the late 1990s, improvements in available digitizer speeds allowed the development of broadband digital INTFs with short ($\sim 1 \mu\text{s}$) recording times that could be triggered multiply during a single flash (Shao et al., 1996; Kawasaki et al., 2000). These instruments took the Fourier transform of signals from multiple antennae to digitally recover the relative phase information. Broadband INTFs can use the higher frequencies in their data-stream to achieve the high angular resolution of a longer baseline narrowband INTF, while using the lower frequencies to remove the phase ambiguity of a narrowband INTF. Despite these advantages, the short recording lengths available for the first broadband INTFs made data interpretation challenging; each VHF event lost the “context” of the entire lightning flash.

More recently (Stock et al., 2014) developed a broadband digital INTF with long continuous recording times (~ 2 s) using cross-correlation to measure time delays between antennas. Long recording times enabled an entire flash to be captured without loss of context caused by gaps in the data set, while cross-correlation removed the “phase-wrap” problem by directly measuring the time-differences between antenna waveforms, making the INTF a short baseline time of arrival (TOA) system. This present study builds heavily on the instrumentation used in Stock et al. (2014) and Stock (2014). The station INTF01 in this study used similar active antennas as Stock with some cost-reduction

63 changes, while the second INTF station (INTF02) used a modified antenna design. Both
 64 stations used Stock’s processing software.

65 Another common method of studying lightning through VHF emissions is with time
 66 of arrival (TOA) instruments, such as those developed by Proctor (1971), Poehler and
 67 Lennon (1979), and Rison et al. (1999). TOA instruments measure the arrival time of
 68 individual pulses at a number of different stations several tens of kilometers apart, and
 69 use the TOA differences to determine the location of the source in 3D space. The Light-
 70 ning Mapping Array (LMA) (Rison et al., 1999) is a widely used TOA instrument. With
 71 a sufficient number of stations and good line of sight the LMA is able to locate sources
 72 over the array to within 12 m_{RMS} horizontally and 30 m_{RMS} vertically (Thomas et al.,
 73 2004).

74 Three-dimensional lightning mapping has also been done with interferometry by
 75 combining angular measurements from two different stations. Mardiana et al. (2002) cre-
 76 ated a three-dimensional INTF (3DINTF) which they estimated to locate sources within
 77 600 m, and Liu et al. (2018) estimated their 3DINTF was accurate within 500 m. These
 78 3DINTFs used segmented recording rather than the continuous recording used in the present
 79 study. Hare et al. (2018) have also used a VHF radio telescope, the Low Frequency Ar-
 80 ray (LOFAR), to map lightning with accuracy on the order 1 m horizontally and 10 m
 81 vertically (Hare et al., 2020). 3D lightning mapping instruments exist at lower frequen-
 82 cies as well, notably the Huntsville Alabama Marx Meter Array (HAMMA) (Bitzer et
 83 al., 2013) operating at 1 Hz to 400 kHz, the Fast Antenna Lightning Mapping Array (FALMA)
 84 (Wu et al., 2018) operating at 500 Hz to 500 KHz, and the Position by Fast Antenna (PBFA)
 85 instruments of Stolzenburg, Marshall and Karunarathna et al. (2017).

86 1.2 New Contributions

87 In this paper we will go into some detail on the analysis procedure of one of the
 88 first continuous 3D interferometers (3DINTF) and verify its accuracy against a collocated
 89 LMA. We will also derive time and space-resolved velocity profiles of repeated K lead-
 90 ers and dart leaders and speculate on what they teach us about leader physics. It thus
 91 behooves us to also review what is known about dart and K Leaders.

92 1.3 Dart Leaders and K Leaders

93 1.3.1 Terminology

94 Dart Leaders and K leaders are fast lightning leaders that retrace channels previ-
 95 ously created by slower leaders in virgin air. Kitagawa (1957) coined the term K change
 96 (K for “Kleine”, or small) to describe an electric field change signature which he suggested
 97 was caused by the same process as a dart leader. (K changes appear as a smaller ver-
 98 sion of the return stroke field change that occurs when lightning strikes the ground.) Lead-
 99 ers associated with K changes are often called K leaders or K-processes waves (Winn et
 100 al., 2011). Despite the recognized equivalence of the physics behind K leaders and dart
 101 leaders (Kitagawa, 1957; Shao et al., 1995), a distinction continues to be made in the light-
 102 ning community with the general understanding that a dart leader progresses to ground
 103 while a K leader remains in the clouds. This distinction is somewhat blurred by authors
 104 who refer to failed or attempted dart leaders which do not reach the ground (Shao et
 105 al., 1995; Rhodes et al., 1994). It seems clear that there should be a common name which
 106 encompasses all such events if the physics behind them is believed to be the same. In
 107 search of a common name some authors refer to all such activity as recoil leaders/streamers
 108 (Akita et al., 2010; Mazur, 2016), or retrograde leaders (Edens et al., 2012). We suggest
 109 to make the term dart leader encompass all leaders of this type, since it was the first term
 110 used to describe this phenomenon, it is descriptive of their high velocity, it is agnostic
 111 of the detailed physical mechanism which is not yet well established, and it can be in-

112 clusive of both retrograde leaders on positive channels as described by Edens et al. (2012),
 113 or prograde leaders on negative channels as observed by Shao et al. (1995). (K leaders
 114 could perhaps be called IC dart leaders if it is necessary to specify that they are not fol-
 115 lowed by a return stroke.) However, until the community reaches a new consensus, we
 116 will use existing terminology. In this paper, we analyze two K leaders followed by three
 117 dart leaders; all using parts of the same channel.

118 **1.3.2 Properties of Dart Leaders and K Leaders**

119 Dart leaders were identified as early as the 1930's by Schonland et al. (1935) us-
 120 ing a Boys camera, where two dimensional average velocities were found to range from
 121 1×10^6 m/s to 23×10^6 m/s, an order of magnitude or two higher than stepped lead-
 122 ers. Further studies of dart leaders are rather consistent with these velocities. Table 1
 123 shows dart leader velocity reported in selected papers, along with some K leader veloc-
 124 ities, which fall in the same range. Schonland et al. (1935) also reported that slower dart
 125 leaders corresponded with longer intervals between return strokes. This observation was
 126 corroborated also by Loeb (1966) and Shao et al. (1995), and in laboratory analogues
 127 (Winn, 1965).

Paper	Leader Velocities (m/s)	leader type
(Schonland et al., 1935)	1×10^6 to 23×10^6	Dart
(Loeb, 1966)	2×10^6 to 20×10^6	Dart
(Jordan et al., 1992)	6×10^6 to 50×10^6	Dart
(Shao et al., 1995)	1×10^6 to 10×10^6	Dart
(Stock et al., 2014)	3×10^6 to 17×10^6	K leader
This study	2×10^6 to 20×10^6	Dart & K

Table 1. The range of maximum and minimum dart (and K) leader velocities reported by selected studies, and compared to this study.

128 Several studies have reported evidence of dart leaders slowing down as they prop-
 129 agate. In the laboratory, analogues of dart leaders exhibited an effect of the ionization
 130 waves slowing down as they propagated along the channel (Winn, 1965). In the field,
 131 Jordan et al. (1992) used a streak camera to study triggered lightning in New Mexico
 132 and Florida and calculated the average velocity of two short segments of the observed
 133 channel near the ground. Jordan found that in New Mexico dart leaders tended to slow
 134 down as they approached ground but in Florida they tended to speed up. Schonland et
 135 al. (1935) also observed that dart leaders in natural lightning tended to slow down as
 136 they approached the ground. Stock et al. (2014) used LMA data to interpolate 3D lo-
 137 cations from 2D INTF sources. Stock et al. observed, on average, that K leaders accel-
 138 erated briefly after initiation and decelerated as they progressed down their channels.

139 **2 Methods**

140 **2.1 Instrumentation**

141 This study used two INTF stations separated by 16 km. The first station (INTF01)
 142 was located at a site designated West Knoll at Langmuir Laboratory, at an altitude of
 143 3.16 km. This station is set as the origin for Easting and Northing for all of the plots
 144 in this paper. INTF01 sampled at 180 MS/s, with the data stream band limited to 20-
 145 80 MHz with a combination of analog and digital filters. Three active flat-plate anten-

nas were used, which effectively act as short-vertical dipoles. The antennas were arranged in an isosceles triangle with two 25 m legs and one 22 m leg. The INTF01 was time synchronized by comparing arrival times with a GPS-synchronized LMA as described in more detail in section 2.3.2.

The second station (INTF02) was located at the airport in Magdalena, New Mexico, at an altitude of 2.05 km. This station was located 13 km north and 9 km west from the INTF01. The INTF02 was developed as a next generation INTF (Stanley et al., 2020), and was only deployed in New Mexico for a short time for testing. As a result the data presented in this study is purely opportunistic, although we are building another INTF for a permanent 2-station setup in the future. The INTF02 sampled at 360 MS/s and had an analog bandwidth of 20-150 MHz, but for this study we digitally bandlimited it to 20-80 MHz to more closely match the INTF01. (This oversampling/bandwidth-limiting had the additional benefit of offering a signal-to-noise reduction.) INTF02 consisted of seven “inverted-v” dipole active antennas modified from the design used by the Long Wavelength Array (LWA) (Ellingson et al., 2013), using the LWA pre-amplifiers. Only three antennas were used in this study, in an isosceles triangle with two 24 m legs and one 32 m leg. The INTF02 was time synchronized by injecting the GPS 1 pulse per second (PPS) directly into the data stream on a high order bit.

2.2 3D Interferometry

Raw data was first processed separately using three antennas at each station to calculate azimuth and elevation angles according to the methods outlined by Stock et al. (2014) and Stock (2014). Cross-correlation is used to measure the time of arrival difference between each pair of antennas. The time of arrival difference between any two antennas determines the source angle as

$$\cos \alpha = \frac{c\tau_d}{d} \quad (1)$$

where α is the incident angle relative to the baseline between the two antennas, c is the speed of light, τ_d is the difference in time of arrival, and d is the distance between the two antennas. (Equation (1) is only strictly true for a plane wave, but it is a good approximation for spherical wavefronts when the distance to the source is much greater than the baseline length.) For a set of three antennas arranged in a triangle independent angles α and β can be calculated. These uniquely give the direction to a source, but not its range. From α and β azimuth and elevation may be readily calculated.

Azimuth and elevation angles from two different INTF stations can be combined using the triangulation method as detailed by Thyer (1962) and Liu et al. (2018). A similar method was used by Mardiana et al. (2002). The triangulation algorithm, along with additional details for different station configurations, are included in Appendix A. The triangulation method gives a 3D location for a source given an azimuth and elevation angle measured from two different locations. In any two station method, there is an additional challenge in determining which sources on each station have a correspondence. In the analysis presented here, we found a correspondence for about half of the detected sources at station 1. Station 2 detected about twice as many sources as station 1. We believe that the antenna and pre-amp design differences discussed in section 2.1 should allow INTF02 to have a better signal to noise ratio than INTF01, but there may be other factors contributing to this difference. This is an ongoing area of investigation.

For a source detected by both stations the maximum possible time of arrival difference is determined by

$$T = D/c \quad (2)$$

where D is the distance between stations and c is the speed of light. For the two INTF stations used, separated by 16 km, that time is 53 μ s. We achieved source matching between the stations by calculating the triangulated locations for every possible pair of sources

194 between the two stations that are separated by 53 μs or less. The source time correspond-
 195 ing to each trial location was calculated using equation 3.

$$t_0 = t_1 - \frac{\sqrt{(x_0 - x_1)^2 + (y_0 - y_1)^2 + (z_0 - z_1)^2}}{c}. \quad (3)$$

196 In equation 3, t_0 , x_0 , y_0 , and z_0 are the source time and position for the trial location,
 197 and t_1 , x_1 , y_1 , and z_1 are the time of arrival and position for one of the antennas (the
 198 choice is arbitrary). Antenna positions were determined by GPS and surveying, while
 199 time-of arrival is determined by the GPS-disciplined time stamp of each acquired data
 200 sample.

201 We then determined the best match by calculating a goodness-of-fit parameter,

$$\chi^2 = \sum_{i=1}^N (t_i^{obs} - t_i^{fit})^2 \quad (4)$$

202 where t_i^{obs} is the observed time of arrival at the i -th antenna, t_i^{fit} is the time of arrival
 203 corresponding to the trial location, and N is the number of antennas. The trial location
 204 that gave the lowest χ^2 value was chosen as the best match location. Best matches were
 205 first identified for every source from INTF01, so that each source from INTF01 was matched
 206 to only one source from INTF02. Best matches were then determined for every remain-
 207 ing INTF02 source so that no source from either station would be included in more than
 208 one match in the final set.

209 We then further refined the 3D locations by using a minimization algorithm to cal-
 210 culate the source location corresponding to the minimum χ^2 value as given by Equation
 211 (4), similar to the method described in Thomas et al. (2004, 2000) for the LMA. The re-
 212 sults in this paper used the Gauss-Newton algorithm for minimization, but later process-
 213 ing with the Levenberg-Marquardt algorithm (used by Thomas et al.) yielded similar
 214 results. In the comparison with the LMA (discussed in Section 2.3.3) minimizing χ^2 only
 215 improved the accuracy by about 10% versus triangulation alone, but we are retaining
 216 this step because modeling suggests that it will lead to further accuracy increases with
 217 improvements in calibration. (These improvements include obtaining centimeter accu-
 218 rate relative antenna locations between stations, and using identical GPS time synchron-
 219 ization at both stations.)

220 **2.3 3DINTF Validation**

221 **2.3.1 Time correction on INTF01**

222 INTF01 data was synchronized with network time, which provided an accuracy of
 223 roughly $\sigma = \pm 4$ ms, however 3DINTF requires timing accuracy of order 100 ns or bet-
 224 ter. A high-precision GPS attached to one of the digitizer channels of the INTF could
 225 provide such accuracy, but none was present for this study. Fortunately, through a syn-
 226 chronization of INTF pulse and LMA pulse arrival times, INTF time can be corrected
 227 using the LMA as a reference. This same procedure also results in a set of points which
 228 can be used to check the accuracy of the 3DINTF. Details of this synchronization scheme
 229 will be discussed in section 2.3.2.

230 **2.3.2 INTF to LMA correlation**

231 To verify the validity of the 3DINTF locations and estimate location accuracy we
 232 compare 3DINTF and LMA source locations for a set of four flashes. Matching of LMA
 233 and INTF data was carried out as follows:

234 The LMA data used had already been processed by well-established code which turns
 235 time-stamped VHF pulses into located data points that are time-stamped with the time

236 of emission at the source location. Since the goal of LMA/INTF correlation is to locate
 237 INTF points at which initially only a time of arrival at an INTF antenna is known,
 238 the LMA source times are updated to the times at which each source would arrive at the
 239 selected INTF antenna.

240 Raw VHF data from the selected single INTF antenna was processed with a 60-
 241 66 MHz forward-backward (zero-phase) Butterworth filter of net order $N=2$. The filtered
 242 INTF signal is now analogous to the raw LMA receiver data. A Hilbert transform was
 243 next applied to produce a power envelope. The largest peak power in a fixed $40 \mu s$ win-
 244 dow is then recorded along with its time stamp. Since the LMA only records peak pow-
 245 ers in fixed windows, the INTF and LMA peaks are assumed to correspond to the same
 246 source. This is true often enough for the technique to work. The pairwise time differ-
 247 ence between all INTF VHF peaks and all LMA arrival times is plotted in a histogram
 248 with one microsecond bins. An initial time offset estimate is determined by taking a weighted
 249 average of the histogram peak and neighboring bins. Once the first time offset is calcu-
 250 lated, a linear regression between LMA and INTF source times is calculated to produce
 251 a refined time offset.

252 Having corrected INTF time with the previous processing step, the strongest INTF
 253 pulse in a $40 \mu s$ window is determined and a time match to an LMA source within one
 254 microsecond is sought. Matches are added to the pulse-pair list. Once a pulse-pair list
 255 is available, it is filtered to keep only the pairs which were also 3D located by the INTF.
 256 The LMA locations on this filtered list can now be directly compared against the 3DINTF
 257 locations. These results are illustrated by Figures 1 and 2.

258 **2.3.3 Determining Accuracy of 3DINTF**

259 In the procedure described above the LMA was used only to correct the station time
 260 on INTF01. Fundamentally, the LMA measurement and the 3DINTF measurements are
 261 independent. Thus the matched INTF/LMA pulse pairs derived as per section 2.3.2 can
 262 be used to verify the accuracy of the 3DINTF method. Figure 1 illustrates the (mostly)
 263 good agreement between the LMA locations (red) and the independently calculated INTF
 264 locations (blue) for the flash to be analyzed in this paper. There is an obvious dispar-
 265 ity visible in panel d between 3 and 6 km northing. It shows LMA (red) sources going
 266 to ground that are not visible in INTF data. These are likely altitude errors resulting
 267 from the limited number of LMA stations. The INTF, in this case, is correct in NOT
 268 detecting them. There is also a burst of INTF (blue) points southeast of the origin not
 269 shown by the LMA. In this case, we hold the 3DINTF matching algorithm responsible.
 270 Picking the wrong match point results in a time error which becomes a range error.

271 Cropped histograms of the discrepancy in each coordinate direction and the over-
 272 all discrepancy between the 3DINTF and the LMA are shown in Figure 2. (The uncropped
 273 histograms are included in the supplementary information in order to verify that we are
 274 only excluding long thin tails. (Jensen et al., 2021)) Overall the distances between match-
 275 ing 3DINTF and LMA points were roughly log-normally distributed, with a median er-
 276 ror of about 220 m. (A log-normal distribution has a normally distributed logarithm.)
 277 To better quantify these errors the absolute median deviation was calculated for each
 278 distribution in Figure 2. The result is 90 m for Easting, 80 m for Northing, and 130 m
 279 in altitude. The absolute median discrepancy is reported rather than a root mean square
 280 (RMS) value because the median is less affected by the extremely long tails. These tails
 281 may be caused by spurious and improper matches between the data sets. The LMA only
 282 had 8 stations operating, with many sources only located by 6 or 7 stations, and the storm
 283 was on the outside edge of the array, so we estimate that the LMA also had errors on
 284 the order of 100-200 m for these flashes. An LMA with 13 or more stations can have RMS
 285 errors as low as 20-30 m for sources over the array (Thomas et al., 2004). The small num-
 286 ber of LMA stations in operation and uncertainty in matching between the 3DINTF and

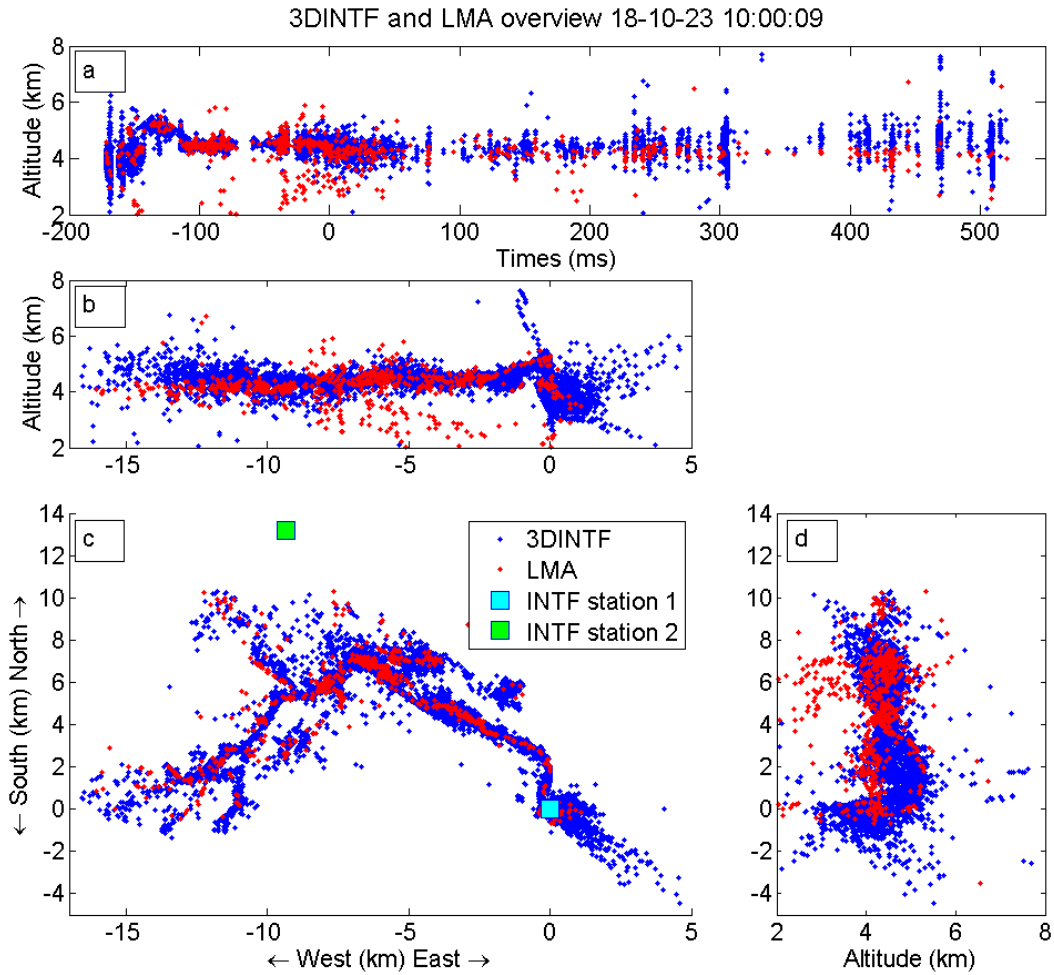


Figure 1. Comparison of 3DINTF and LMA for the 10:00:09 flash on October 23rd, 2018. Plots show altitude vs time (**a**), altitude vs east/west (**b**), north/south vs east/west (**c**), and north/south vs altitude (**d**). 3DINTF sources are marked in blue and LMA sources are in red. See section 2.3.3 for additional discussion of discrepancies between these data sets.

287 LMA means the measured discrepancies only serve as an upper bound on the uncertainty
 288 in the 3DINTF source locations, the true median accuracy may be better than 200 m.
 289 We plan to conduct a more precise measurement of 3DINTF accuracy in the future.

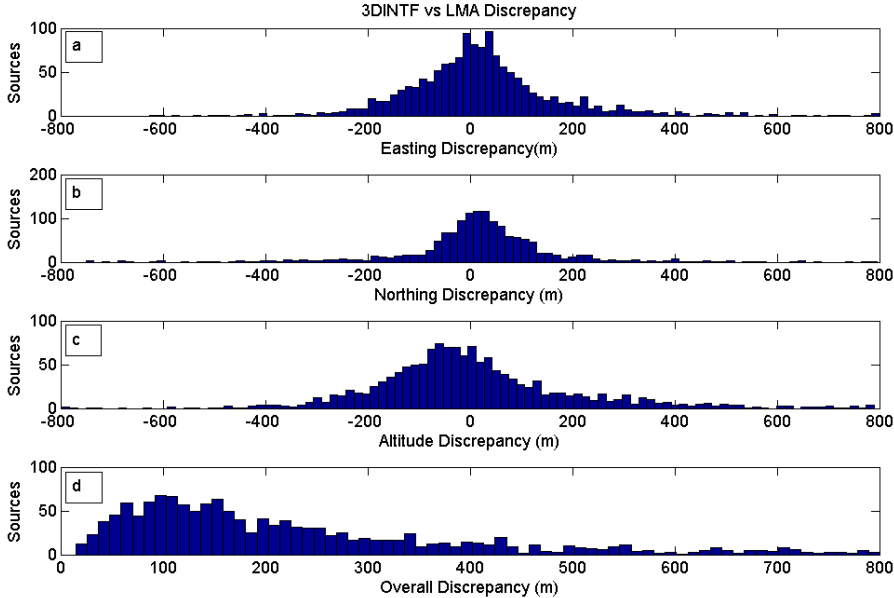


Figure 2. Histograms of the measured discrepancies between matching 3DINTF and LMA source locations, east-west discrepancies (a), north-south discrepancies (b), altitude discrepancies (c), and overall 3D discrepancies (d). Histograms are cropped to 800 m because this range includes 80% of the data, the remaining 20% are distributed in thin tails out as far as 16 km.

2.4 Velocity Estimation

290
 291 The set of sources in the dart/K leaders displayed a change in position that was
 292 generally monotonic in time and there was little VHF activity on other channels dur-
 293 ing their occurrence. This allowed a simple rolling average (boxcar window) to be used
 294 to filter that leader’s position vs. time. The values for each coordinate were calculated
 295 as:

$$\bar{x}_1(i) = \frac{1}{N} \sum_{k=i}^{i+N} x(k) \quad (5)$$

296 where N is the number of points averaged over, $x(k)$ is the k -th data point in the set of
 297 x coordinates for sources in the leader, and $\bar{x}_1(i)$ is defined as the x -coordinate for the
 298 i -th point in the leader, \bar{x} being a traditional way to denote the average. The y , z , and
 299 time coordinates of the leader were smoothed in the same way. In order to estimate the
 300 velocity these coordinates were compared to the next N points, with coordinates defined
 301 as $\bar{x}_2(i) = \bar{x}_1(i + N)$ and the velocity was calculated as

$$v_1(i) = \frac{\sqrt{(\bar{x}_2(i) - \bar{x}_1(i))^2 + (\bar{y}_2(i) - \bar{y}_1(i))^2 + (\bar{z}_2(i) - \bar{z}_1(i))^2}}{\bar{t}_2(i) - \bar{t}_1(i)} \quad (6)$$

302 Several different values N were tested. $N = 40$ was found to be a good balance between
 303 channel tracking and noise rejection.

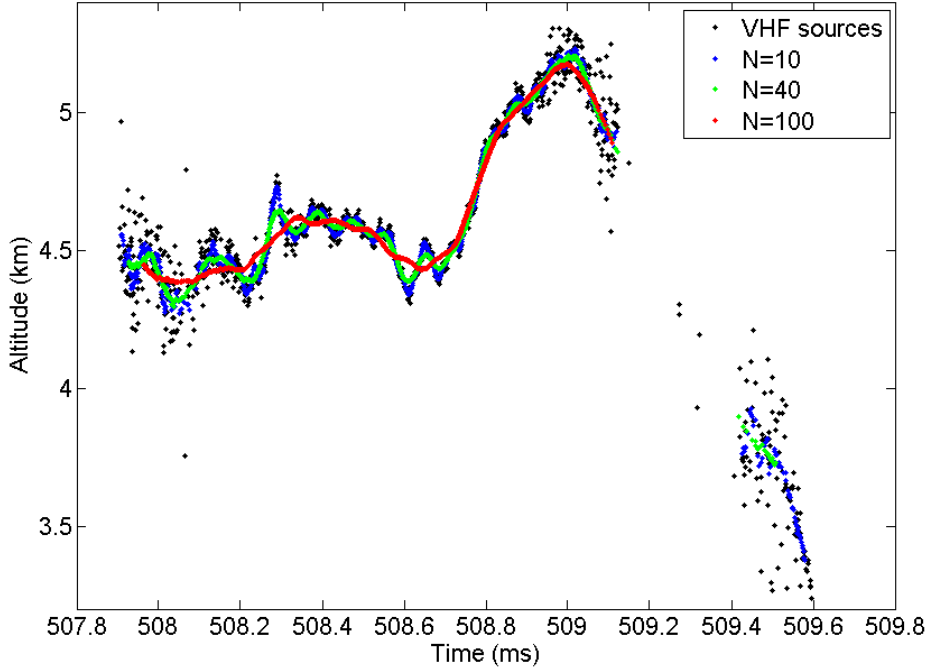


Figure 3. Comparison of rolling averages of the second dart leader using different numbers of points, in a plot of altitude vs time, with the original VHF sources (black) and the rolling average points. Averages are performed using 10 points (blue), 40 points (green), and 100 points (red). The gap in data is caused by a null in antenna sensitivity directly over the INTF01.

304 Figure 3 of altitude vs. time for the third dart leader displayed with various box-
 305 car windows, demonstrates that a smaller window results in truer tracking of the chan-
 306 nel. In contrast, Figure 4 shows that too small a window yields an excessively noisy ve-
 307 locity plot.

308 The fixed N averaging used is approximately equivalent to averaging over a fixed
 309 Δt for this data set. The raw INTF processing used windows $1.4 \mu\text{s}$ long (256 samples
 310 at 180 MS/s), and locates, at most, one source per window. During dart leaders and k
 311 leaders we typically observed sources in every $1.4 \mu\text{s}$ window, meaning the length of the
 312 rolling averaging windows was approximately $N \cdot 1.4 \mu\text{s}$.

313 To calculate the velocity error we first calculated the standard deviation σ_p about
 314 the mean position for each rolling average window. In order to arrive at a value repre-
 315 sentative of the position error of the entire data set the mean of the individual σ_p ($\bar{\sigma}_p$),
 316 was calculated.

317 The mean time difference between consecutive N point windows, $\overline{\Delta t}$ was also found.
 318 As expected, it turned out to be approximately $N \cdot 1.4 \mu\text{s}$. Assuming that the devia-
 319 tions for each window are independent the average 1σ deviation from the true mean ve-
 320 locity $\bar{\sigma}_V$ is then approximately given by Equation (7).

$$\bar{\sigma}_V = \frac{\sqrt{2}\bar{\sigma}_p}{\overline{\Delta t} \sqrt{N}} \quad (7)$$

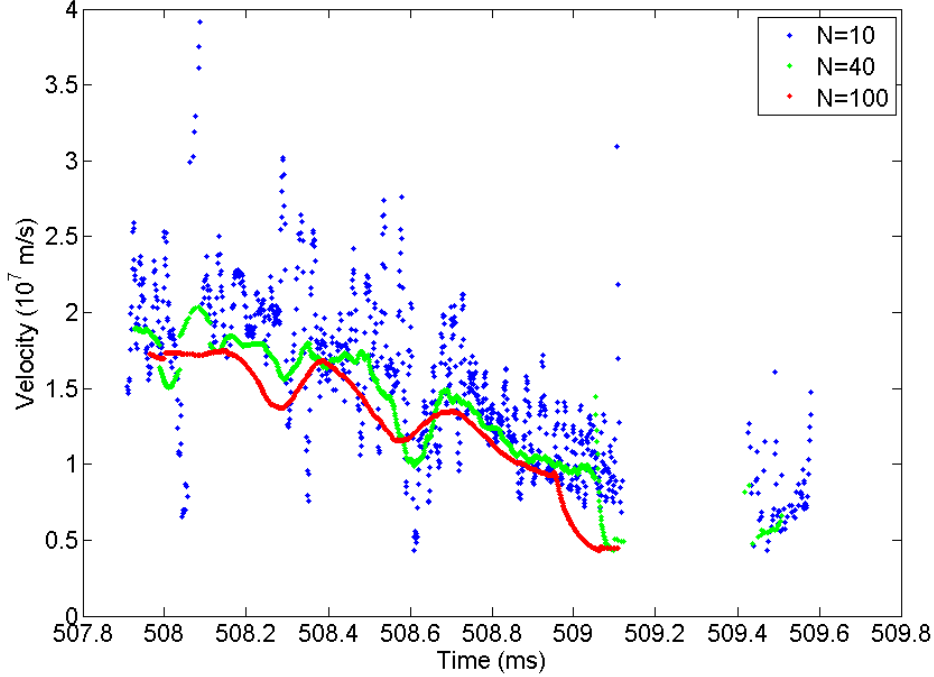


Figure 4. Comparison of different sized rolling averages of the second dart leader on the plots of velocity vs time. Averages are performed using 10 points (blue), 40 points (green), and 100 points (red). The gap in data is caused by a null in antenna sensitivity directly over the INTF01.

N	$\bar{\sigma}_p$ (m)	$\bar{\sigma}_p/\sqrt{N}$ (m)	$\overline{\Delta t}$ (μ s)	$\bar{\sigma}_V$ (m/s)
10	60.8	19.2	13.4	2.0×10^6
40	132	20.9	55.4	0.53×10^6
100	266	26.6	139.7	0.26×10^6

Table 2. A summary of values used in estimating the 1σ deviation from the true average velocity. Note that $\overline{\Delta t}$ is indeed approximately $N * 1.4$ microseconds.

321 The values of $\bar{\sigma}_p$, $\bar{\sigma}_p/\sqrt{N}$, $\overline{\Delta t}$, and the estimated 1σ errors $\bar{\sigma}_V$ are summarized in Ta-
 322 ble 2. Since we recommend $N = 40$ as a good compromise between tracking accuracy
 323 and velocity error, we suggest viewing the green curve in Figure 4 assuming an error bar
 324 of $\simeq \pm 5 \times 10^5$ m/s.

325 Gaps in the data in Figures 3 and 4 between 509.1 ms and 509.4 ms are caused by
 326 a null in antenna sensitivity directly over the INTF01. Averaged points are removed if
 327 they are not within 1μ s of a real VHF source to prevent averaging over such gaps.

328 3 Results

329 3.1 Charge Region Identification

330 Figure 5 shows charge regions identified from LMA data for flashes happening near
 331 Langmuir Lab between 09:50:00 and 10:20:00 UTC on 2018-10-23. Charge regions were

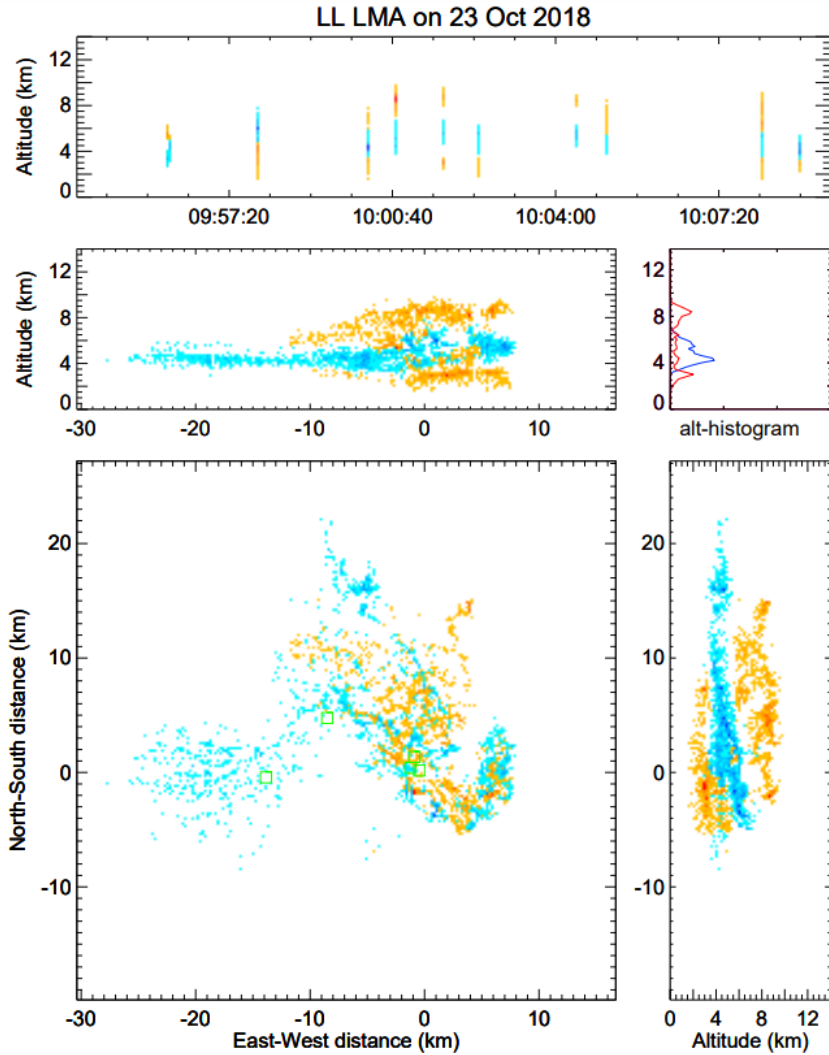


Figure 5. Charge structure as identified by the LMA for flashes happening between 09:50:00 UTC and 10:20:00 UTC near Langmuir Lab on 2018-10-23. Negative charge is shown as blue, positive as orange/red.

332 identified following the procedure outlined by Hamlin et al. (2003); Krehbiel et al. (2008).
 333 The plot shows the tripolar structure typical of many thunderstorms, as described by
 334 Williams (1989) and Marshall et al. (2005). The lower positive region appears to be around
 335 2.5-3.5 km above mean sea level (MSL), the main negative region appears to extend from
 336 roughly 4 km to 6 km, and the upper positive region is spread from 6 km to 9 km MSL.
 337 The altitudes of these regions are significantly lower than those observed by Marshall
 338 et al. (2005) and Edens et al. (2012), but this is to be expected as their observations were
 339 made in July and August, and this paper discusses results from a storm in late October.
 340 The charge regions are known to be defined by temperature rather than altitude
 341 (Krehbiel, 1986), and with lower temperatures at the ground in late October we would
 342 expect the charge regions to be lower in altitude.

343 There is no reason 3DINTF data couldn't be used to perform a similar charge analysis
 344 in the future, but the data is not currently compatible with the existing tools for
 345 the LMA. Figure 6 shows a histogram of the altitudes of 3DINTF sources from 10:00:00 UTC

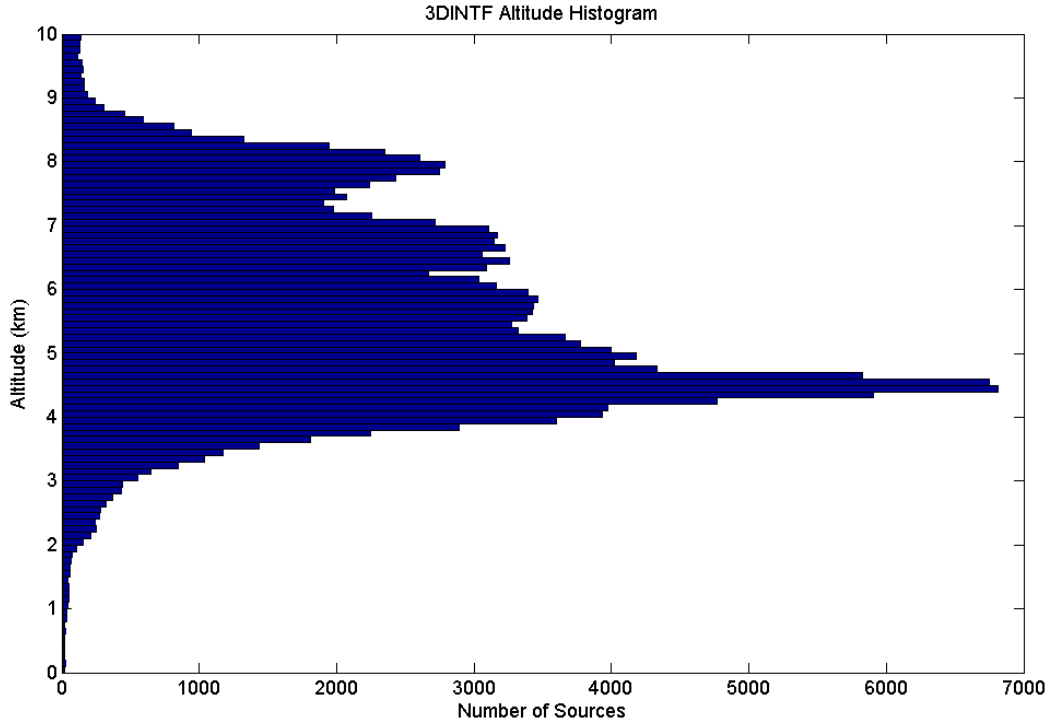


Figure 6. A histogram of 3DINTF VHF source altitudes for flashes happening between 10:00:00 UTC and 10:20:00 UTC near Langmuir Lab on 2018-10-23

346 to 10:20:00 UTC. The upper positive (6 km to 9 km MSL) and main negative (4 km to
 347 6 km MSL) charge regions identified by the LMA are also visible in the 3DINTF data,
 348 and their rough extent can be identified from the histogram alone, assuming the storm
 349 has a normal tripolar structure. The lower positive region is not obviously present in the
 350 3DINTF histogram, but we have only processed 4 flashes for the 3DINTF in this time
 351 period, while Figure 5 was compiled from 11 flashes where the charge structure could
 352 be easily identified. (There were 43 flashes in all in this time period.) It is reasonable
 353 to suppose the 3DINTF histogram would be closer to the charge structure identified by
 354 the LMA if more flashes were included from the chosen interval. The LMA and individ-
 355 ual INTF stations did detect a similar number of flashes, but as these are initial results
 356 and we have not yet developed an efficient processing pipeline we only fully processed
 357 the 4 flashes which looked most promising based on the INTF01 data alone. The LMA
 358 data for Figure 5 was processed with $80 \mu\text{s}$ windows and limited to at least seven partic-
 359 ipating stations for each source. The data set consists of just under 18,000 sources be-
 360 tween the 43 flashes. The 3DINTF, by contrast, captured over 172,000 sources between
 361 just the 4 processed flashes. With an average flash duration of around 1 second this trans-
 362 lates to a detection rate of approximately 40,000 sources per second, although this is a
 363 very small number of flashes to sample. We hope to get closer to the detection rate of
 364 the individual INTF stations with future processing improvements.

3.2 Flash Development

3.2.1 Flash Overview

In all the plots that follow, the origin of the coordinate system ($X=0$, $Y=0$) is located at station INTF01. The INTF02 station was located 13 km north and 9 km west from the INTF01. The measurements were performed in mountainous terrain. The altitude of the two interferometers is 3.16 km and 2.05 km respectively.

Figure 7 gives an overview of the entire lightning flash of interest. The data is presented in the style of an LMA Plot, which has become a familiar way of displaying three-dimensional data (Thomas et al., 2004). As described in section 2.3.2, an LMA was used to check the validity of the 3DINTF mapping, but all the 3D locations shown here are solely INTF results. Other than the charge structure plot in Figure 15, no further data obtained from the LMA is presented in this paper.

We first present an overview to orient the reader, and then return to discuss the flash in more detail stroke by stroke. (For a more complete picture of the flash development please refer to the animation included in the supplementary material (Jensen et al., 2021).) The flash begins with two cloud-to-ground (CG) strokes, visible as nearly vertical features in 7a (before -150 ms, colored dark blue). The National Lightning Detection Network (NLDN) (Cummins et al., 1998) also identifies negative CGs at this time (indicated by diamonds in the plots). The second of these CG's is most likely preceded by a dart leader since it appears to go to ground near the same place as the first, but the 3DINTF mapping of the channel in this region is inadequate for useful analysis. Thus we will not discuss this dart leader further in our analysis. (Also, we deemed it less confusing to not count this missed dart leader in our numbering scheme. Thus when we say "first dart leader" we really mean "first well-resolved dart leader" in what follows. This "missed leader" does not, in our view, impact the conclusions of this paper.)

The negative charge brought to ground in the initial -CGs results in a pocket of reduced negative charge in the region above the CG grounding locations. It is thus energetically favorable for a positive leader to issue horizontally from this reduced negative charge into the main negative charge, and this is precisely what is shown in the blue/yellow/red data points that move west from the origin in Figure 7b. (Many of these points are covered by the brick red points of dart leaders that occur later in the flash). Once this positive leader has reached a point roughly seven km west of the origin, a negative K leader travels back along the horizontal channel. (This K leader begins around $t=-40$ ms, and should be coloured blue, but is likewise buried beneath the brick red data points from later dart leaders.) The positive leader resumes its extension with blue to green data points (-40 ms through 230 ms), and there is another negative K leader at $t=230$ ms. Positive leader growth then continues with the yellow and orange points until the first resolved dart leader occurs around $t=310$ ms. After the first dart leader, the positive leader continues to grow, leading to a second dart leader at 470 ms, and a third one at 510 ms. Both the NLDN and 3DINTF data suggest that all of the CGs in this flash go to ground at approximately the same location, on the mountain top just east of the INTF01, which is at an altitude of 3.16 km. Having understood the big picture, let us look at each of these sections in more detail.

3.2.2 Blooming and Channel Tracking

As this paper gets deeper into detailed discussions of flash development, it is helpful to define a new term, "blooming". It has been our observation that RF source data (both LMA and INTF) sometimes shows a clear channel, and in the case of an INTF sometimes shows an exceedingly clear subsequent channel (which we discuss further below). Sometimes however, the time development of RF appears more as a cloud of points. While sometimes these are noise, at other times we believe they reflect the development

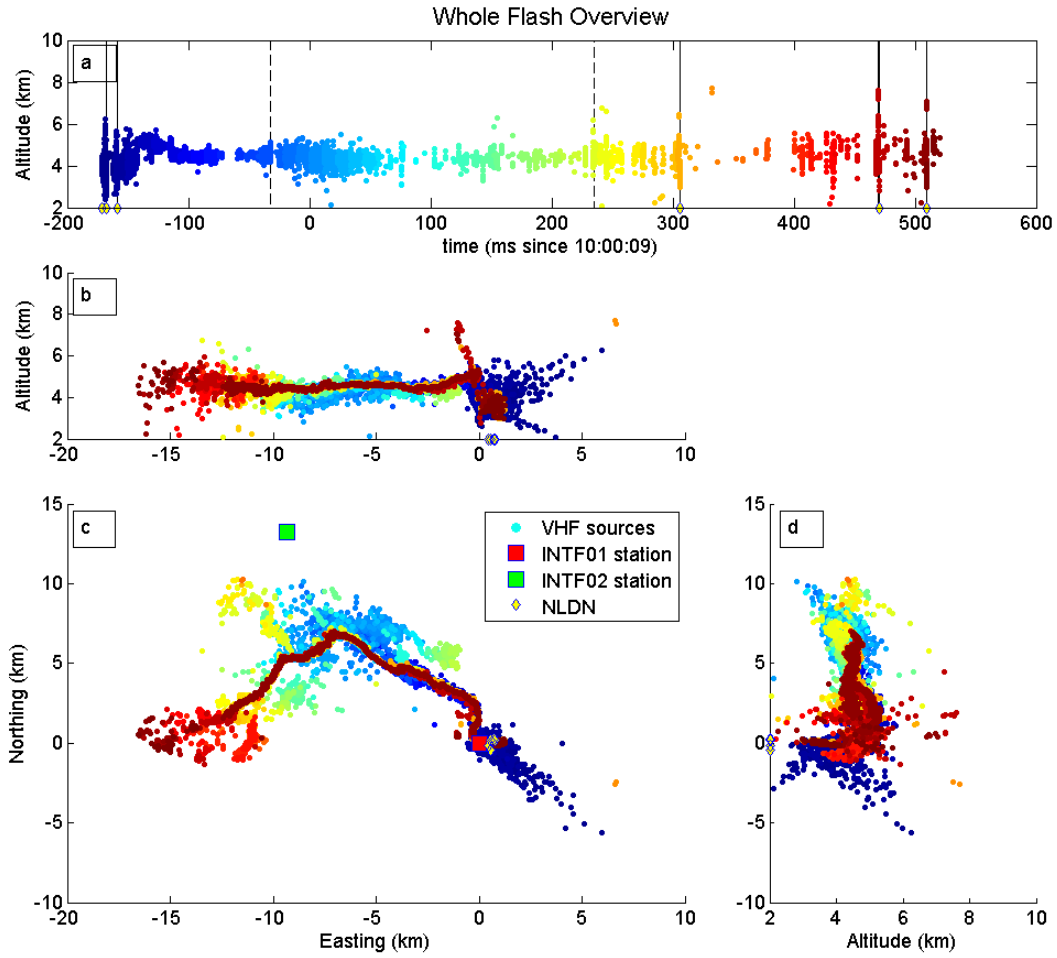


Figure 7. Overview of the entire flash from 10:00:09 UTC on 2018-10-23, with sources colored blue to red according to time. (a) altitude vs. time, (b) altitude vs. east/west position, (c) Plan view (north/south vs. east/west), (d) altitude vs. north/south position. The 3DINTF VHF sources are shown along with the location of the INTF01 and INTF02 stations, and the time and location of NLDN strokes. (In panel c, the NLDN ground-strike points are immediately to the east of INTF01). Dashed vertical lines in (a) are 3DINTF IC strokes, solid lines are CG strokes (on which the NLDN and 3DINTF agree).

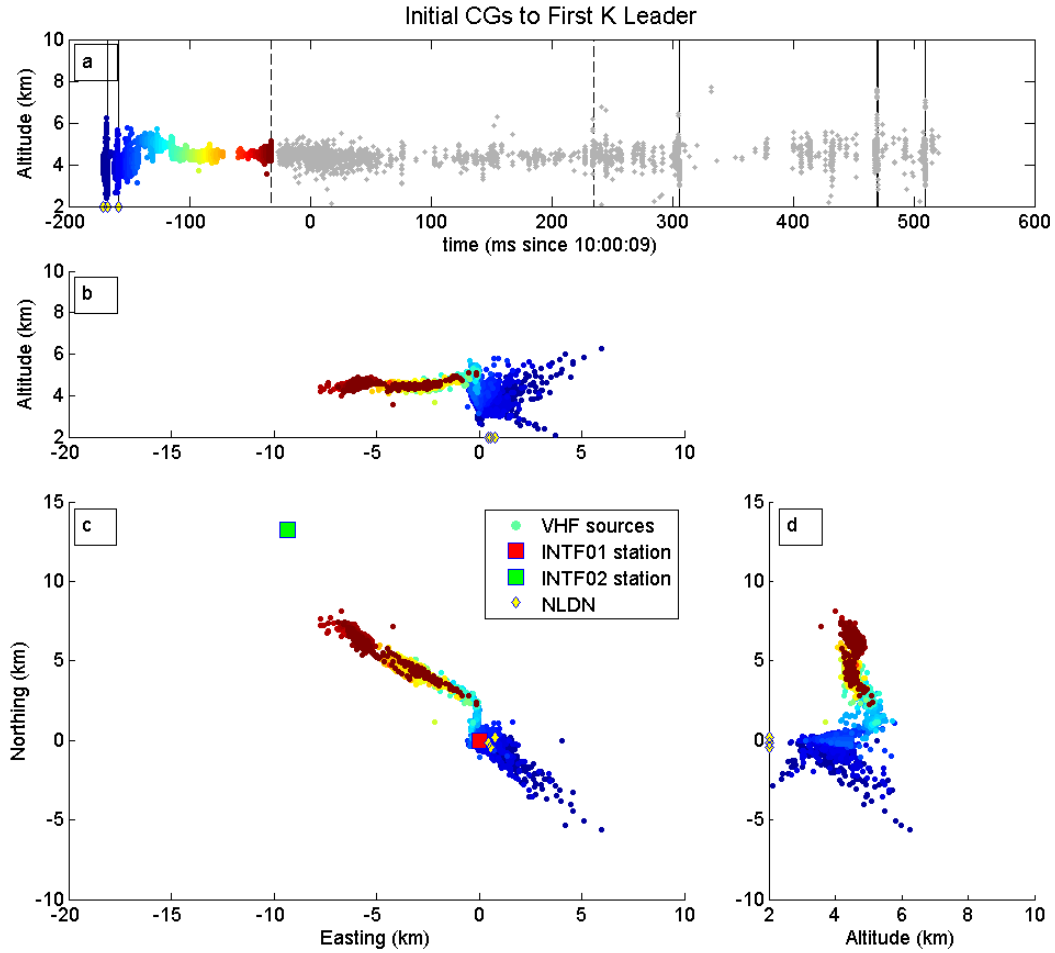


Figure 8. The beginning of the flash up to the first K leader. Sources colored blue to red according to time. (a) altitude vs. time, (b) altitude vs. east/west position, (c) Plan view (north/south vs. east/west), (d) altitude vs. north/south position. The 3DINTF VHF sources are shown along with the location of the INTF01 and INTF02 stations, and the time and location of NLDN strokes (yellow diamonds). Dashed vertical lines in (a) are 3DINTF IC strokes, solid lines are CG strokes.

415 of a highly branched channel or a channel with many leader tips that are active at al-
 416 most the same time. We refer to this phenomenon in which the channel grows in many
 417 directions at once where they are not clearly resolved by the instrument as “blooming”.
 418 It is purely descriptive. We are not attributing new physics to it. Researchers who have
 419 looked at fast videos, may have noted that for some flashes only one or two tips on a chan-
 420 nel are active, but some branches may have a dozen or more optically active sub-branches
 421 or leader tips at once. These would be barely resolved by an INTF and may well be what
 422 an INTF sees as “blooming”.

423 **3.2.3 K Leaders**

424 Figure 8 shows the development of the flash up to the first K leader, with sources
 425 colored by time. After the two initial negative CGs near the origin the positive leader
 426 propagates primarily to the northwest (in panel c). This positive leader appears to re-
 427 main in a single well defined channel until about -40 ms, when the first K leader begins.
 428 (The K-leader is shown in brick red in Figure 8b,c,d.)

429 After the first K leader the positive leader resumes propagation, and begins bloom-
 430 ing into many branches as seen in Figure 9. There are clear large branches to the north-
 431 west, east, and south-west, as best seen in Figure 9c. The branch to the north-west de-
 432 velops into the second K leader, which reaches roughly the same point along the chan-
 433 nel as the first K leader. Again, the K-leader shows up as a well-defined channel of brick
 434 red points within the more scattered branches of the positive leader.

435 **3.2.4 Dart Leaders**

436 Figure 10 shows continued blooming in the north-west and south-west branches of
 437 the positive leader, leading to the first dart leader just after 300 ms. The NLDN reports
 438 a negative CG at this time, which is consistent with this being a negative leader prop-
 439 agating back down a channel initially created by positive breakdown.

440 Figure 11 shows further blooming of the positive leader, primarily in the south-west
 441 branch, which leads to a second dart leader around 470 ms, again the NLDN reports a
 442 negative CG at this time.

443 Figure 12 shows further positive leader growth in the south-west branch, and the
 444 third dart leader around 510 ms, following quite quickly after the second dart leader at
 445 470 ms. This dart leader is also coincident with an NLDN negative CG.

446 **3.3 Reduced “branching” of dart leaders and K leaders**

447 Having discussed the flash in detail, a feature of the data in Figure 7 and the sub-
 448 sequent dart and K leader figures should be remarked upon. Back at Figure 7, panels
 449 b and c clearly show a brick-red dart leader (the final one) overlaying the earlier pos-
 450 itive leader points. In fact, that final dart leader overlays the earlier ones so completely
 451 that they cannot be seen. This fact will be useful in our forthcoming velocity calcula-
 452 tions, but is itself of note. The great deal of “scatter” or “blooming” visible on all the
 453 VHF sources preceding the dart leaders is *not* a result of poor location precision. Rather,
 454 it seems to be characteristic of the much more highly branched nature of leaders into vir-
 455 gin air on the 100-1000 m scale, as compared to dart leaders.

456 Hare et al. (2019) have observed that all of the positive leader sources they see with
 457 LOFAR are actually “needles”, which are negative breakdown propagating away from
 458 the positive channel some distance behind the tip. From this it seems likely that the ma-
 459 jority of positive leader sources observed by any similar VHF systems, including the 3DINTF
 460 and the LMA, are in fact from needles. If the needles do not emit VHF as a dart leader

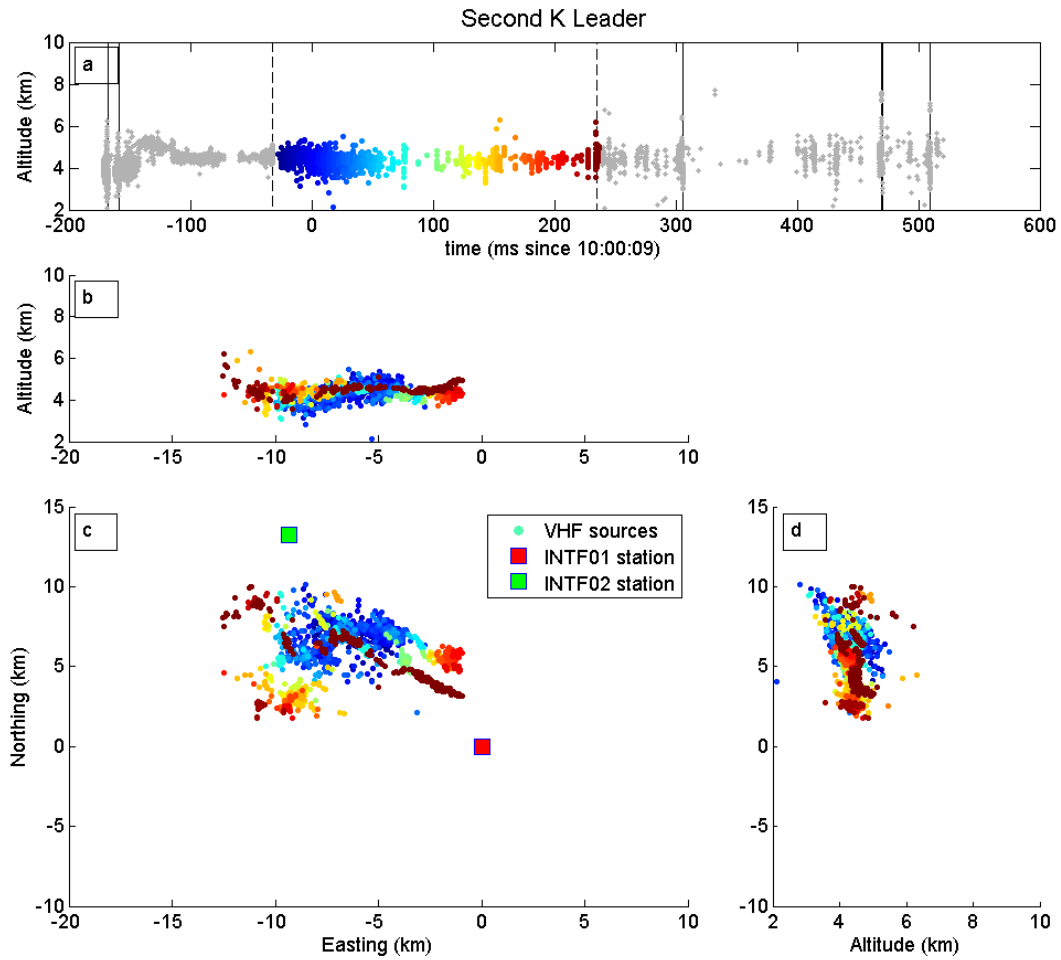


Figure 9. Overview of the second K leader and leader growth that precedes it. Sources colored blue to red according to time. (a) altitude vs. time, (b) altitude vs. east/west position, (c) Plan view (north/south vs. east/west), (d) altitude vs. north/south position. The 3DINTF VHF sources are shown along with the location of the INTF01 and INTF02 stations. Dashed vertical lines in (a) are 3DINTF IC strokes, solid lines are CG strokes.

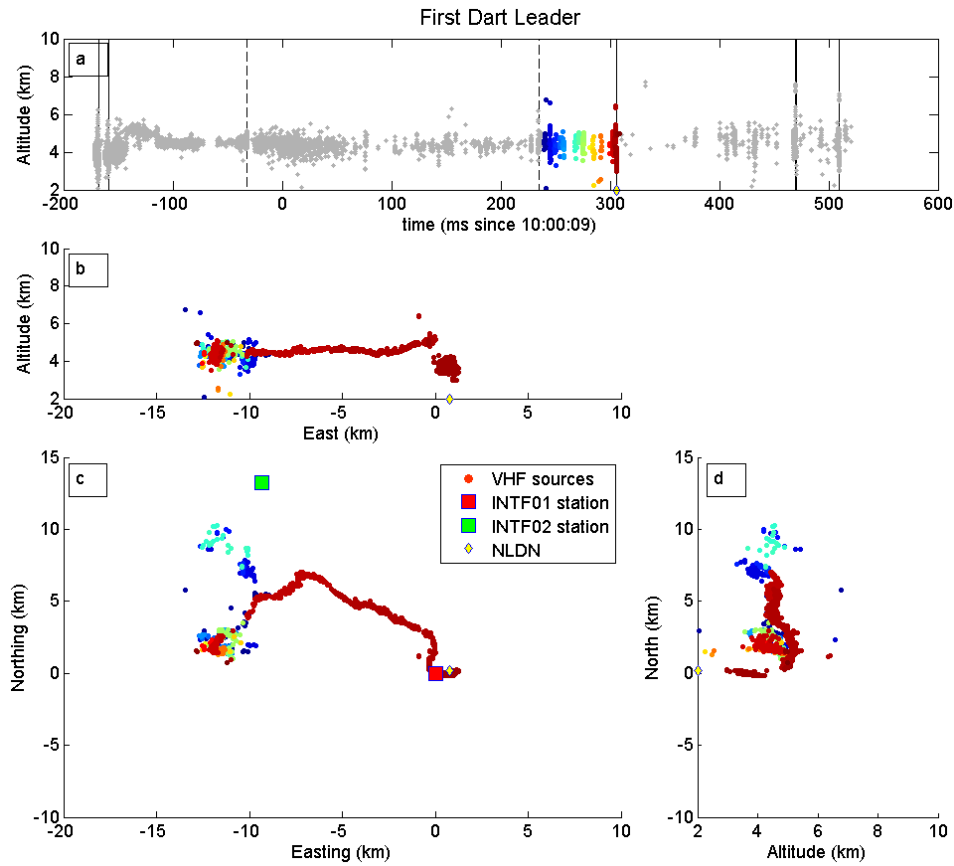


Figure 10. Overview of the first dart leader and the blooming that precedes it, with sources colored blue to red according to time. (a) altitude vs. time, (b) altitude vs. east/west position, (c) Plan view (north/south vs. east/west), (d) altitude vs. north/south position. The 3DINTF VHF sources are shown along with the location of the INTF01 and INTF02 stations, and the time and location of NLDN strokes. Dashed vertical lines in (a) are 3DINTF IC strokes, solid lines are CG strokes.

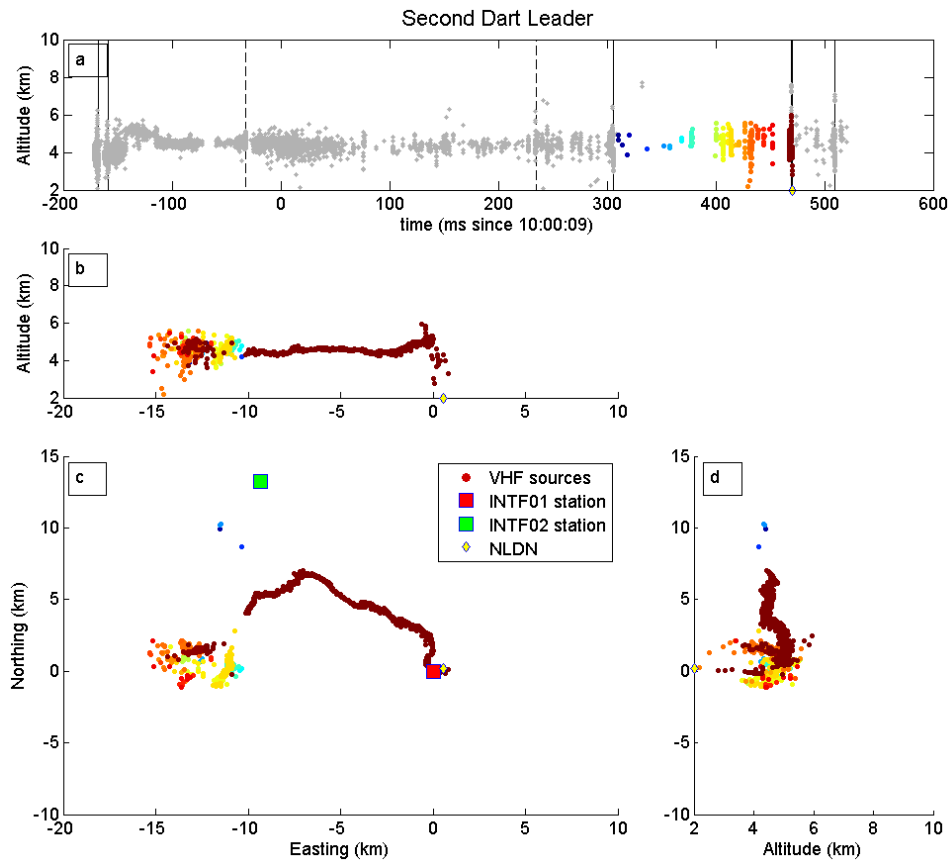


Figure 11. Overview of the second dart leader and the blooming that precedes it, with sources colored blue to red according to time. (a) altitude vs time, (b) altitude vs. east/west position, (c) Plan view (north/south vs. east/west), (d) altitude vs. north/south position. The 3DINTF VHF sources are shown along with the location of the INTF01 and INTF02 stations, and the time and location of NLDN strokes. Dashed vertical lines in (a) are 3DINTF IC strokes, solid lines are CG strokes.

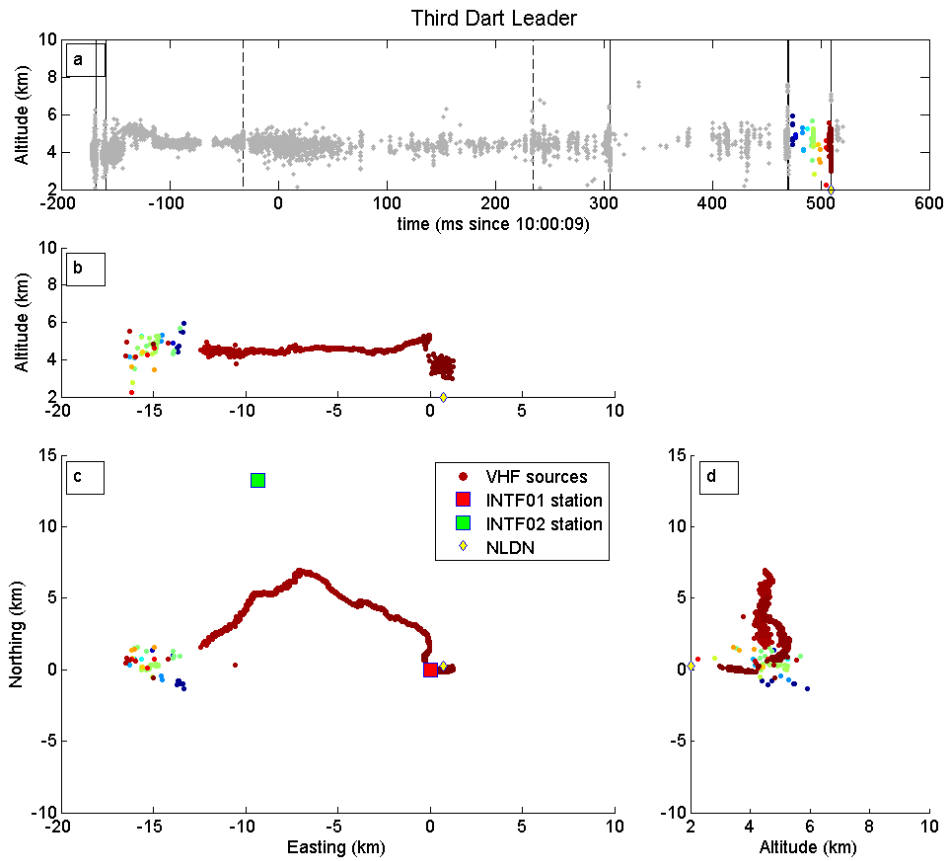


Figure 12. Overview of the third dart leader and the blooming that precedes it, with sources colored blue to red according to time. (a) altitude vs time, (b) altitude vs. east/west position, (c) Plan view (north/south vs. east/west), (d) altitude vs. north/south position. The 3DINTF VHF sources are shown along with the location of the INTF01 and INTF02 stations, and the time and location of NLDN strokes. Dashed vertical lines in (a) are 3DINTF IC strokes, solid lines are CG strokes.

461 passes their connection to the channel (as observed by Hare et al. (2020)) this would largely
 462 explain the difference in observed channel width, for positive leaders.

463 It is not yet clear whether the 3DINTF observes VHF sources from the positive leader
 464 tip as well, or only from the needles. Stanley et al. (2020) showed that the INTF02 (us-
 465 ing its full 140 MHz bandwidth and 6 antennas) clearly observes both needles and the
 466 positive leader tip, but similar results have not yet been shown for the older INTF01 sys-
 467 tem. Small branches near the leader tip were observed by Ding et al. (2020) for nega-
 468 tive leaders. Here we may see them on a positive leader. (We do not claim to resolve any
 469 structure within the scattered leader sources.) This phenomenon of reduced width has
 470 long been noted with video observations of dart leaders proceeding to ground.

471 We want to clarify that it is *also* characteristic of the in-cloud portion of dart lead-
 472 ers, as well as K leaders. We suggest that this reduced branching tells us something about
 473 the physics of a dart leader and that it is somehow a preferred path for the re-ionization
 474 wave. Similar observations were reported by Shao et al. (1995) and seen in the results
 475 of Stock et al. (2014).

476 3.4 Velocity

477 Velocities for both K leaders and all three dart leaders are shown in Figure 13, while
 478 Figure 14 shows how the channel segments were aligned. The velocity of each dart or
 479 K leader was integrated over time to give a distance along the channel at each point, and
 480 the initial offsets of these integrated distances were adjusted so that the shared portions
 481 of each dart leader channel would align in the original spatial coordinates (altitude, nor-
 482 thing, and easting), as shown in Figure 14. The zero point was arbitrarily chosen to be
 483 the beginning of the final dart leader. Figure 14 demonstrates that, for most of their length,
 484 all the K leaders and dart leaders share the same three-dimensional path. The leaders
 485 were aligned in this way in order to show how the velocity at each point along the chan-
 486 nel varied between the K leaders and dart leaders. Some obvious trends appear, most
 487 notably the large dip in velocity around 11 km, which occurs in every dart and K leader
 488 that passed that point. The second K leader, which is already traveling slowly as it passes
 489 the location of the dip, is the only exception to this behavior. A smaller dip is also ap-
 490 parent in all three dart leaders at around 6.5 km (Figure 13). While we do not under-
 491 stand what is special about the locations of the speed dips, it seems that there is some
 492 reproducible feature (presumably related to overall charge structure of the storm) which
 493 causes the dips to occur repeatedly at the same location in the thundercloud.

494 The calculated velocities range from 2×10^6 m/s to 20×10^6 m/s. This agrees
 495 very well with the range of velocities other researchers have reported, as listed in Table 1.
 496 With the exception of the first K leader, which started very quickly and then dropped
 497 off again, the other 4 leaders generally increased in velocity with each subsequent pass
 498 along the channel. This is consistent with the channel being increasingly conditioned by
 499 previous leaders and return strokes (Behnke et al., 2005; Rakov & Uman, 1990), although
 500 the first K leader shows that there must be multiple factors that determine the veloc-
 501 ity of dart leaders and K leaders. Bazelyan and Raizer (1997) hints at a possible mech-
 502 anism for conditioning in equation 2.17 and his statement that negative Oxygen ions re-
 503 quire only 0.5 eV for reionization. Our data provide more clear examples of this poorly
 504 understood phenomenon.

505 3.5 Why does leader velocity decrease along the channel?

506 Figure 13 clearly shows velocity decreasing as the leaders progress along the chan-
 507 nel, similar to the behavior Behnke et al. (2005) saw in initial leaders, but now in the
 508 context of dart and K leaders. We can think of three mechanisms which could lead to
 509 the observed velocity decreases. The first mechanism we will discuss is increasing pres-

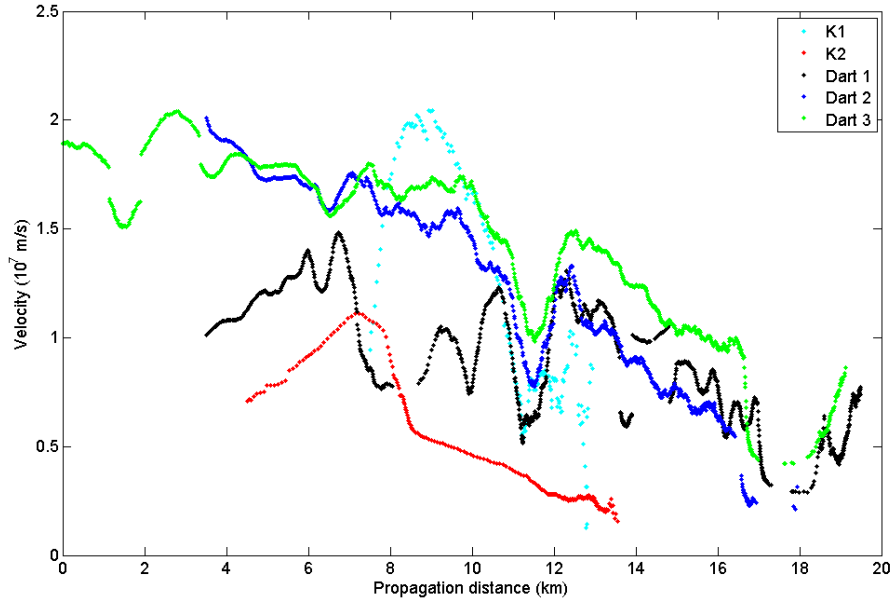


Figure 13. Plot of velocity versus distance propagated along the channel for all of the dart leaders and K leaders. Showing K leader 1 (cyan), K leader 2 (red), dart leader 1 (black), dart leader 2 (blue), and dart leader 3 (green). Zero propagation distance is arbitrarily set to be the start of the last dart leader.

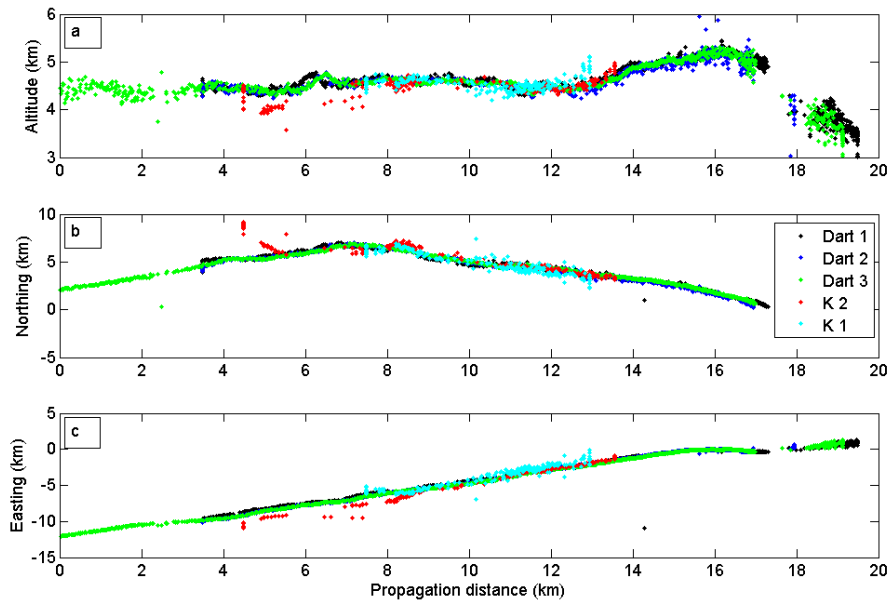


Figure 14. Plot showing how the channel segments were aligned for each dart leader and K leader. Showing K leader 1 (cyan), K leader 2 (red), dart leader 1 (black), dart leader 2 (blue), and dart leader 3 (green). Zero propagation distance is arbitrarily set to be the start of the final dart leader. The gap between 17-18 km is caused by a null in antenna sensitivity directly above the INTF01 station.

510 sure as the leader propagates toward ground. Based on mean-free-path considerations,
 511 the leader might be expected to slow because of increased pressure (da Silva & Pasko,
 512 2013).

513 However there are two reasons to reject the pressure/speed hypothesis. First, it was
 514 previously shown that for negative stepped leaders descending from 10 km to ground the
 515 step length decreased with altitude, but the average velocity did not decrease. The step
 516 rate increased inversely with the step length (Edens et al., 2014). The second reason to
 517 reject the pressure/speed hypothesis is that roughly the first 10 km of channel progresses
 518 at a relatively constant 4.5 km of altitude (Figure 14a), while the next 5 km increases
 519 in altitude to 5 km. Thus, if there is any pressure effect on speed, we might expect a speed-
 520 up, contrary to observation. This suggests that pressure is not the driver of leader speed
 521 change for most of the leader.

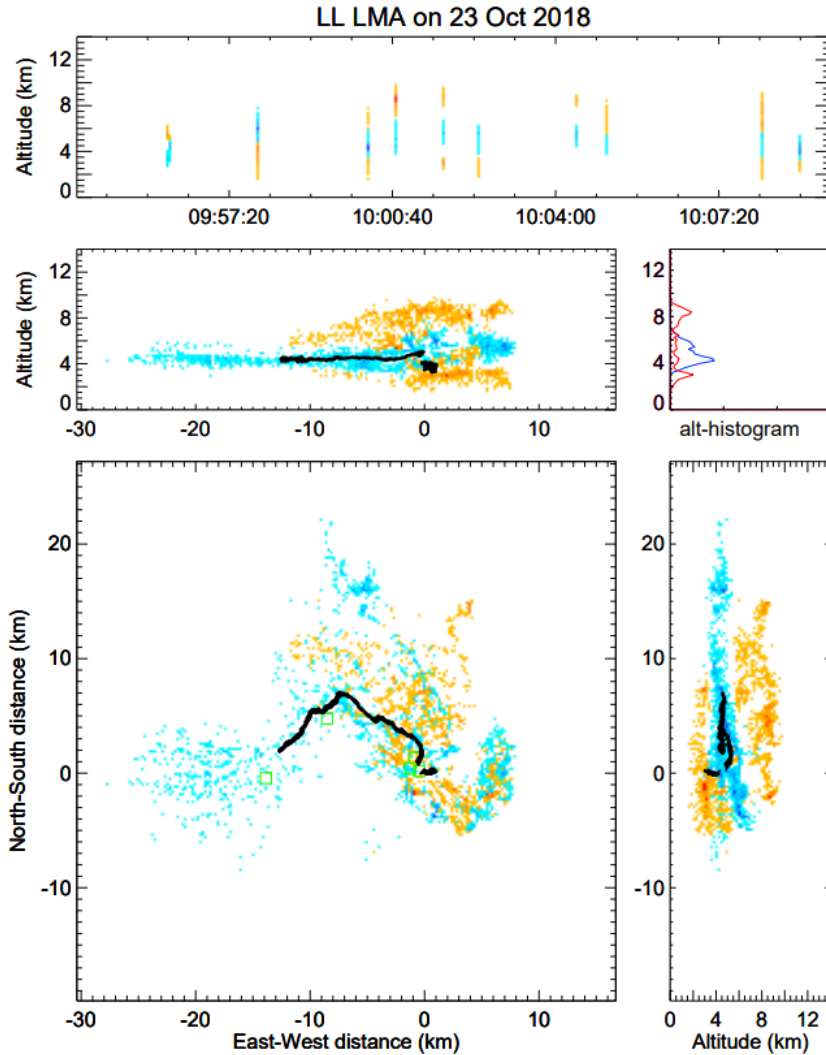


Figure 15. Charge structure as identified by the LMA for flashes happening between 09:50:00 UTC and 10:20:00 UTC near Langmuir Lab on 2018-10-23. Negative charge is shown as blue, positive as orange/red. The path of the dart leaders in the 10:00:09 flash is overlaid in black.

522 The second explanation for speed change along the channel would be a change in
 523 local macroscopic field. It would be very exciting to have 3D interferometry in concert

524 with quantitative background field mapping of the thunderstorm – but this falls under
 525 the realm of future work. We can only take an educated guess of where local fields might
 526 be high based on the LMA data for the storm.

527 Figure 15 is an LMA charge analysis for the 20 minute period surrounding the flash
 528 of interest (see section 3.1). The Altitude vs. East-West panel of this figure shows that
 529 the eastern region of the storm piles VHF sources to a substantially higher altitude than
 530 the western region. Also, around zero kilometers Easting the trilayer charge structure
 531 becomes very apparent. The non-inductive charging theory for thunderstorms connects
 532 strong updraft regions with the charging engine. Absent other data, we would think that
 533 the updraft engine is operating fiercely right around zero kilometer E–W and that the
 534 ambient fields might be higher in this region. We have overlaid the path of the dart lead-
 535 ers on top of the LMA data points in black. Figure 15 demonstrates that the dart lead-
 536 ers and K leaders progress from the western extremities of the storm into the eastern re-
 537 gion of putatively higher fields. We would naively expect leaders to speed up as they en-
 538 tered higher ambient fields. To the extent that our extrapolations are correct, this sec-
 539 ond hypothesis for speed change of the leader fails as well.

540 What remains with highest probability is the third explanation; in which we con-
 541 sider a dart leader as a guided nonlinear ionization wave in a decaying plasma channel
 542 (See Bazelyan and Raizer (2000), Section 4.8). In this framework, the rate of electron-
 543 impact and thermal ionization dictates how quickly a new leader section can be formed
 544 (da Silva & Pasko, 2013), and thus the dart leader speed is proportional to the magni-
 545 tude of the electric field created at the leading crest of this soliton. (Like a soliton, these
 546 leader tips are isolated pulses in a highly non-linear system with limited dispersion.) This
 547 high electric field is needed to reionize the decaying channel. As energy is spent reion-
 548 izing the channel, the magnitude of the leading edge electric field decays, and *so does*
 549 *its velocity*. A similar process happens in streamer discharges (Naidis, 2009).

550 Please note that this is *different* than the transmission line interpretation of a light-
 551 ning channel. In a transmission line, the amplitude of the wave decays as a function of
 552 distance due to the existence of a finite resistance. The wave velocity is a function of the
 553 inductance, capacitance, resistance, and frequency content of the wave packet (Rakov,
 554 1998). However for a constant resistance (the assumption of transmission line models),
 555 there should be a constant velocity, i.e. it does *not* decrease.

556 One might wonder about the source and sink of the reionization energy? This is
 557 not well understood so we will make a hypothesis. Once initiated with some initial en-
 558 ergy (by a process which is still not understood), a dart leader continues to be fed by
 559 the ambient electrostatic environment. This results in a concentration of charge at the
 560 leader tip which also represents electrostatic energy. Some of this energy is spent in ion-
 561 ization at the leader tip and is seen as charges left behind on the re-ionized channel. If
 562 the energy fed by the environment is insufficient for the expenditure on ionization, the
 563 leader field would decrease and the leader could slow, as observed.

564 3.6 Systematic Error

565 For the 3DINTF there is an extreme amount of scattering in the source locations
 566 associated with the initial CGs (shown in dark blue in Figures 7 and 8). This is most
 567 likely caused by poor matching in this region as individual branches of the downward
 568 leader were well resolved by the INTF01 but not by the INTF02, because the flash started
 569 essentially directly overhead of the INTF01. The INTF01 antennas also have a null in
 570 their sensitivity at 90° overhead so there were gaps in the detected sources, and more
 571 work needs to be done to precisely measure the relative orientation of the two arrays.

572 It is not clear if the large dip in velocity around 11 km in Figure 13 is a real sig-
 573 nal or simply a systematic error. There is no obvious increase in scattering of sources

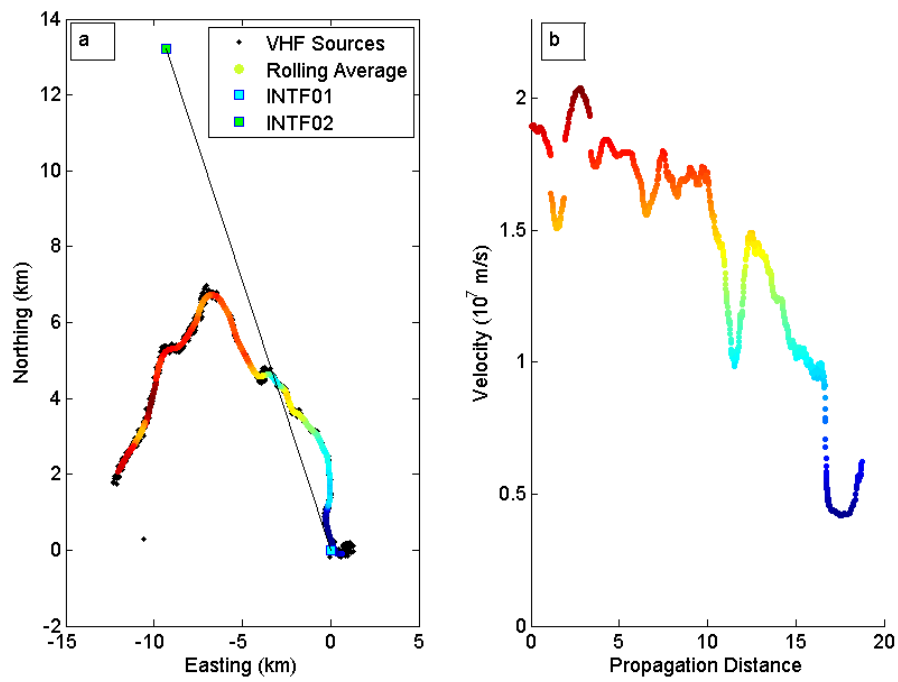


Figure 16. Plot showing the correspondence between the large dip in velocity at about 11 km along the channel and the baseline between the two INTF stations for the second dart leader. North/south and east/west location of sources and stations (a), and velocity vs propagation distance (b). Sources are colored by velocity.

574 for any of the dart leaders or K leaders that pass through this region to indicate that
 575 the dip is caused by increasing location error, but it is suspicious that the dip occurs al-
 576 most exactly along the baseline between the two INTF stations. Figure 16 highlights the
 577 location of the dip along the third CG dart leader by coloring points by velocity rather
 578 than the standard time coloring. The location of the velocity dip in Figure 16a can eas-
 579 ily be identified as the channel color changes from yellow, to green, to blue, and back to
 580 yellow in a short period, which coincides with the point where the line between INTF01
 581 and INTF02 crosses the channel. Location errors for the Triangulation method can be
 582 increased along this line as small changes in measured azimuth lead to large differences
 583 in the calculated range to the point, but this would be expected to manifest as a signif-
 584 icant broadening of the channel along this line, which does not appear to be the case.
 585 The third dart leader is shown in the plot. As we previously pointed out, all 3 dart lead-
 586 ers and the K leader exhibiting this dip in speed have it at the same channel location.

587 All three dart leaders have a smaller dip in velocity at 6.5 km along the channel
 588 (Figure 13), at a point with no obvious geometrical significance. Along with the lack of
 589 scattering, this suggests that these variations may be real. Further evidence is seen in
 590 the fact that the second K leader does not exhibit a dip in velocity when it passes through
 591 the same point in the channel. If the drop in velocity was a geometrical artifact then it
 592 would be expected to show up for any leader passing through that point. Thus we con-
 593 clude that the observed variations likely reflect true changes in velocity at these points,
 594 although further observations and modeling of processing errors will help to verify this
 595 claim.

596 There is also a significant decrease in velocity in all three dart leaders around 17 km,
 597 and a subsequent increase in velocity between 18 km and 20 km. Since these coincide
 598 with the gap in VHF data directly overhead of the INTF01 and the region of high scat-
 599 ter near the station these trends are almost certainly just artifacts. Flashes which go to
 600 ground further from the INTF01 station will need to be observed in order to study the
 601 characteristics of dart leaders as they approach the ground.

602 4 Conclusions

603 In this paper we have:

604 1. Documented in an appendix a double theodolite location method for 605 use in lightning interferometry

606 The original work (Thyer, 1962) contained a typographical error which left the al-
 607 gorithm ambiguous. We have also extended it to allow for interferometers of non-
 608 zero size (theodolites can be considered to be points!), and for arbitrary config-
 609 urations of the two stations.

610 2. Verified the minimum accuracy of a 2 station 3DINTF

611 Using a two station INTF colocated with a 8-station LMA, we showed that 3DINTF
 612 can have good location accuracy (200 m median error), and sufficient time-resolution
 613 to observe rapid processes like dart leaders and K leaders in detail. In checking
 614 the location accuracy of the INTF for sources located by both instruments, the
 615 LMA was assumed to be “correct”. In fact, for the 8-station LMA used, the LMA
 616 errors might also have been in the 100 m range.

617 3. Shown that charge identification can be done with an INTF

618 The charge layers we identified were consistent with those found by an LMA, though
 619 less complete at this time. We speculate here that, because of the high spatial and
 620 temporal sample density of an INTF, future studies might allow one to observe
 621 the “granularity” of charges in a cloud (in other words, recognizing smaller charge
 622 pockets in addition to the overall layers in a storm).

623 4. Profiled in time and space the velocities of dart leaders and K leaders 624 in the cloud

INTF data rates allow measurement of faster phenomena like dart leaders, which could previously only be observed in detail using optical techniques below clouds.

5. **Observed that average dart leader velocity generally increases with subsequent strokes.**

For all but the first K leader, the average velocity increased with subsequent dart and k leaders on the same channel. This is likely due to channel conditioning.

6. **Noted that dart leader velocity decreases with channel progression**

All dart and K leaders consistently showed 2X-3X velocity decreases as they progressed over 15-20 km. Because so much of these leaders were horizontal, this effect is likely not a pressure effect. We have weak evidence that it is not precisely an effect of storm-level electric field either. Our most likely conclusion is that the velocity decreases as available overvoltage at the channel tip decreases as energy is pumped into ionizing a lengthening column of air.

7. **Observed repeated variations in velocity at fixed points along the channel**

In addition to the general velocity decrease with channel progression our spatially resolved measurements saw a pair of dips in dart-leader propagation speed that were linked to particular locations along the channel. The presence of two of these dips along the dart leader path and the lack of obvious scattering of sources at these locations suggests that they are real observations and not merely artifacts.

8. **Pointed out that dart and K leaders can be recognized in VHF images by relative lack of branching**

This result is apparent from high speed video. It is also apparent in INTF images as reported by Shao et al. (1995), that stepped leaders are much “fuzzier” than subsequent dart leaders. This “fuzz” is likely finely branched channels or needles which are not reionized in the second pass of a dart leader. This would make sense if the over-voltage needed for reionization is lower because of a chemical conditioning process.

Appendix A Triangulation: The Double Theodolite Method

This algorithm is taken from Thyer (1962) and Liu et al. (2018). It was decided to reproduce a large portion of their work as a service to the community because (Thyer, 1962) contains a typographical error, corrected here. New also herein is a generalization to arbitrary station locations and an allowance for the non-zero size of each interferometer. The algorithm determines the points of closest approach between the “line of sight” of the two stations (defined by their azimuth and elevation measurements). Figure A1 shows a diagram for the location process. The source location is chosen along the line between the points of closest approach. The point is weighted to be closer to the line of sight of the station that is closer to the source, to satisfy

$$\frac{DS}{SC} = \frac{AD}{BC} \quad (\text{A1})$$

where AD is the distance between points A and D as shown in Figure A1, BC is the distance between points B and C, DS is the distance between points D and S, and SC is the distance between points S and C.

For an INTF station with 3 antennas, the antennas form a plane. There is a line perpendicular to this plane where the relative time of arrival will be the same at all three antennas for any source on the line. The point where that line intersects the plane of the antennas is the circumcenter of the triangle defined by the antennas. The reported azimuth and elevation angles have an origin at the circumcenter. For the triangulation algorithm the circumcenter of each station is the location for the A and B points. For stations with more than 3 antennas there is not in general a well defined center. The azimuth and elevation measurements are also not well defined in general for more than 3

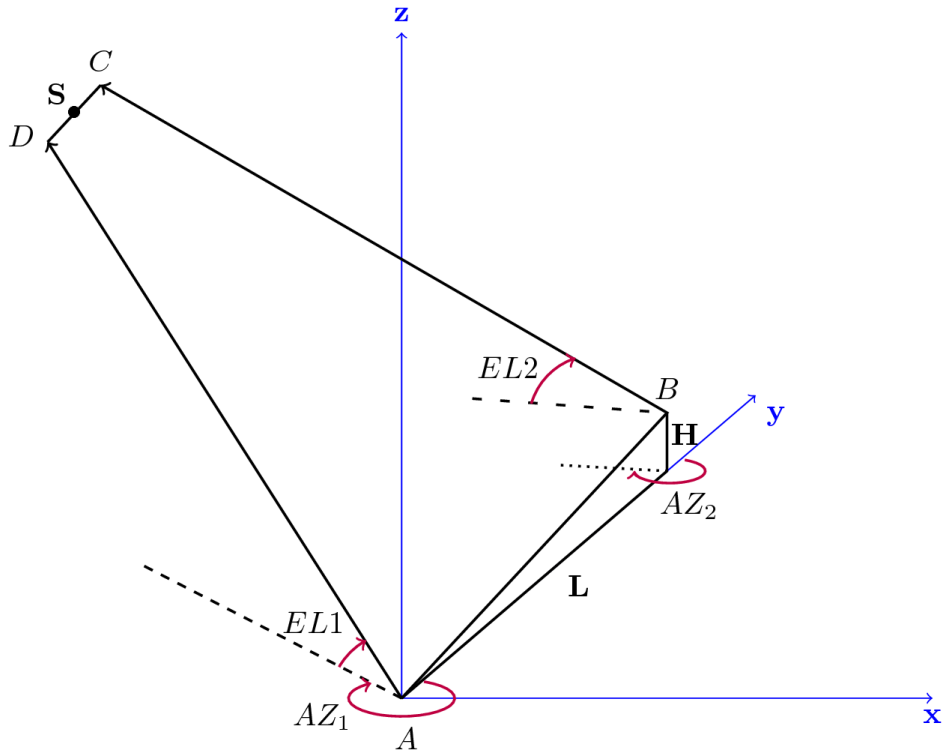


Figure A1. A diagram inspired by (Liu et al., 2018) for the double theodolite triangulation, showing station 1 (A), station 2 (B), their azimuth and elevation measurements (AZ_1 , EL_1 , and AZ_2 , EL_2). Point D is the point of closest approach along the line of sight for station 1, and point C is the point of closest approach along the line of sight from station 2. Point S is the source location.

675 antennas since there is a different origin for every combination of 3 antennas. However,
 676 for an array that is small relative to the distance to the source, the difference in angle
 677 measured from the different origins may be smaller than the uncertainty in each angle
 678 measurement caused by other sources of error. Additional antennas are also useful if a
 679 least squares minimization method is applied after triangulation.

680 The double theodolite algorithm assumes that the second INTF station is directly
 681 north of the first. If this is not the case simply calculate the azimuth of the second sta-
 682 tion relative to the first,

$$az_{1 \rightarrow 2} = \tan^{-1} \left(\frac{B_x - A_x}{B_y - A_y} \right) \quad (\text{A2})$$

683 where A_x and B_x are the east-west aligned x coordinates of station 1 and 2 respectively
 684 in linear units (meters, etc.), and A_y and B_y are the north-south aligned coordinates,
 685 and $az_{1 \rightarrow 2}$ is the azimuthal direction of station 2 relative to station 1. The azimuth val-
 686 ues for sources detected by each station should then be shifted as

$$AZ_{shifted} = AZ_{original} - az_{1 \rightarrow 2} \quad (\text{A3})$$

687 to align with the shifted coordinate system.

688 The VHF sources are projected onto a sphere of radius 1 (any units), with x (east),
 689 y (north), and z (altitude) coordinates of

$$x_1 = \cos(EL_1) \sin(AZ_1) \quad (\text{A4})$$

$$y_1 = \cos(EL_1) \cos(AZ_1) \quad (\text{A5})$$

$$z_1 = \sin(EL_1) \quad (\text{A6})$$

690 where EL_1 is the elevation of the source measured from station 1, defined as the angle
 691 measured up from horizontal. AZ_1 is the azimuth angle of the source measured from sta-
 692 tion 1, with zero defined to be north and the angle increasing clockwise when down on
 693 a map view. Similarly we calculate

$$x_2 = \cos(EL_2) \sin(AZ_2) \quad (\text{A7})$$

$$y_2 = \cos(EL_2) \cos(AZ_2) \quad (\text{A8})$$

$$z_2 = \sin(EL_2) \quad (\text{A9})$$

694 for the coordinates relative to station 2.

695 The line connecting the points of closest approach must be perpendicular to both
 696 of the lines of sight, so we calculate the cross product components

$$c_x = z_1 y_2 - y_1 z_2 \quad (\text{A10})$$

$$c_y = x_1 z_2 - z_1 x_2 \quad (\text{A11})$$

$$c_z = y_1 x_2 - x_1 y_2 \quad (\text{A12})$$

$$|\vec{c}| = \sqrt{c_x^2 + c_y^2 + c_z^2} \quad (\text{A13})$$

697 and the normalized cross product components

$$\hat{c}_x = c_x / |\vec{c}| \quad (\text{A14})$$

$$\hat{c}_y = c_y / |\vec{c}| \quad (\text{A15})$$

$$\hat{c}_z = c_z / |\vec{c}| \quad (\text{A16})$$

698 We use the additional quantities of $L = \sqrt{(A_x - B_x)^2 + (A_y - B_y)^2}$ for the hor-
 699 izontal distance between the two stations and $H = B_z - A_z$ for the altitude difference

700 between stations 2 and 1. L and H should be in the same linear units, their units will
 701 determine the units of the final calculated positions. We choose meters. We then cal-
 702 culate the range along the lines of sight to the points of closest approach as

$$R_1 = \frac{L(x_2\hat{c}_z - z_2\hat{c}_x) + H(\hat{c}_xy_2 - x_2\hat{c}_y)}{|\vec{c}|} \quad (\text{A17})$$

$$R_2 = \frac{L(x_1\hat{c}_z - z_1\hat{c}_x) + H(\hat{c}_xy_1 - x_1\hat{c}_y)}{|\vec{c}|} \quad (\text{A18})$$

$$R_3 = \frac{Lc_x + Hc_z}{|\vec{c}|} \quad (\text{A19})$$

703 where R_1 is the distance between station 1 and the point of closest approach along sta-
 704 tion 1's line of sight, and R_2 is the distance between station 2 and the point of closest
 705 approach along station 2's line of sight, and R_3 is the length of the line between the two
 706 points of closest approach.

707 We then calculate the source position as

$$X' = R_1x_1 + \frac{R_3R_1}{R_1 + R_2}\hat{c}_x \quad (\text{A20})$$

$$Y' = R_1x_1 + \frac{R_3R_1}{R_1 + R_2}\hat{c}_y \quad (\text{A21})$$

$$Z' = R_1x_1 + \frac{R_3R_1}{R_1 + R_2}\hat{c}_z \quad (\text{A22})$$

$$(\text{A23})$$

708 where the X' , Y' , and Z' coordinates are relative to the location of station 1.

709 This source location can then be corrected for the coordinate shift that was needed
 710 to align the stations in the y direction, and the altitude can be set relative to sea level,
 711 so the final corrected source locations are

$$X = X' \cos(-az_{1 \rightarrow 2}) - Y' \sin(-az_{1 \rightarrow 2}) \quad (\text{A24})$$

$$Y = X' \sin(-az_{1 \rightarrow 2}) + Y' \cos(-az_{1 \rightarrow 2}) \quad (\text{A25})$$

$$Z = Z' + A_z \quad (\text{A26})$$

712 where $az_{1 \rightarrow 2}$ is calculated in Equation A2. The X and Y coordinates are still relative
 713 to station 1, but it is convenient to have a local reference frame.

714 Acknowledgments

715 We thank Isaac Edelman for assistance with the double theodolite figure.

716 This work has been supported by the NSF EPSCoR Program under award OIA-
 717 1757207, by NSF award AGS-1917069, by Defense University Research Instrumentation
 718 Program award W911NF-16-1-0512, by collaborative grants from Vaisala and Earth Net-
 719 works, by a Centennial Grant from the American Geophysical Union, and by the Australian-
 720 American Fulbright Foundation.

721 The field operations at Langmuir Laboratory were conducted on the Cibola Na-
 722 tional Forest under a Special Use Permit from the U.S. Forest Service.

723 All data supporting our conclusions is publicly available at [http://doi.org/10](http://doi.org/10.5281/zenodo.4561227)
 724 [.5281/zenodo.4561227](http://doi.org/10.5281/zenodo.4561227). (License: Creative Commons Attribution 4.0 International, open
 725 access). (Jensen et al., 2021)

726 References

727 Akita, M., Nakamura, Y., Yoshida, S., Morimoto, T., Ushio, T., Kawasaki, Z., &
 728 Wang, D. (2010). What occurs in k process of cloud flashes? *Journal of*

- 729 *Geophysical Research: Atmospheres*, 115(D7). Retrieved from [https://](https://agupubs.onlinelibrary.wiley.com/doi/abs/10.1029/2009JD012016)
730 agupubs.onlinelibrary.wiley.com/doi/abs/10.1029/2009JD012016 doi:
731 10.1029/2009JD012016
- 732 Bazelyan, E. M., & Raizer, Y. P. (1997). *Spark Discharge*. CRC Press.
- 733 Bazelyan, E. M., & Raizer, Y. P. (2000). *Lightning physics and lightning protection*.
734 CRC Press.
- 735 Behnke, S. A., Thomas, R. J., Krehbiel, P. R., & Rison, W. (2005). Initial leader ve-
736 locities during intracloud lightning: Possible evidence for a runaway breakdown
737 effect. *Journal of Geophysical Research: Atmospheres*, 110(D10). Retrieved
738 from [https://agupubs.onlinelibrary.wiley.com/doi/abs/10.1029/](https://agupubs.onlinelibrary.wiley.com/doi/abs/10.1029/2004JD005312)
739 2004JD005312 doi: 10.1029/2004JD005312
- 740 Bitzer, P. M., Christian, H. J., Stewart, M., Burchfield, J., Podgorny, S., Corredor,
741 D., ... Franklin, V. (2013). Characterization and applications of VLF/LF
742 source locations from lightning using the Huntsville Alabama Marx Meter Ar-
743 ray. *Journal of Geophysical Research: Atmospheres*, 118(8), 3120–3138. doi:
744 10.1002/jgrd.50271
- 745 Cummins, K. L., Krider, E. P., & Malone, M. D. (1998). The us national light-
746 ning detection network and applications of cloud-to-ground lightning data by
747 electric power utilities. *IEEE Transactions on Electromagnetic Compatibility*,
748 40(4), 465-480.
- 749 da Silva, C. L., & Pasko, V. P. (2013). Dynamics of streamer-to-leader transi-
750 tion at reduced air densities and its implications for propagation of lightning
751 leaders and gigantic jets. *Journal of Geophysical Research: Atmospheres*,
752 118(24), 13,561-13,590. Retrieved from [https://agupubs.onlinelibrary](https://agupubs.onlinelibrary.wiley.com/doi/abs/10.1002/2013JD020618)
753 [.wiley.com/doi/abs/10.1002/2013JD020618](https://agupubs.onlinelibrary.wiley.com/doi/abs/10.1002/2013JD020618) doi: [https://doi.org/10.1002/](https://doi.org/10.1002/2013JD020618)
754 2013JD020618
- 755 Ding, Z., Rakov, V. A., Zhu, Y., & Tran, M. D. (2020). On a possible mechanism
756 of reactivation of decayed branches of negative stepped leaders. *Journal of*
757 *Geophysical Research: Atmospheres*, n/a(n/a), e2020JD033305. Retrieved
758 from [https://agupubs.onlinelibrary.wiley.com/doi/abs/10.1029/](https://agupubs.onlinelibrary.wiley.com/doi/abs/10.1029/2020JD033305)
759 2020JD033305 (e2020JD033305 2020JD033305) doi: [https://doi.org/10.1029/](https://doi.org/10.1029/2020JD033305)
760 2020JD033305
- 761 Edens, H., Eack, K., Rison, W., & Hunyady, S. (2014). Photographic observations
762 of streamers and steps in a cloud-to-air negative leader. *Geophysical Research*
763 *Letters*, 41(4), 1336–1342.
- 764 Edens, H. E., Eack, K. B., Eastvedt, E. M., Trueblood, J. J., Winn, W. P., Krehbiel,
765 P. R., ... Thomas, R. J. (2012). Vhf lightning mapping observations of a
766 triggered lightning flash. *Geophysical Research Letters*, 39(19). Retrieved
767 from [https://agupubs.onlinelibrary.wiley.com/doi/abs/10.1029/](https://agupubs.onlinelibrary.wiley.com/doi/abs/10.1029/2012GL053666)
768 2012GL053666 doi: <https://doi.org/10.1029/2012GL053666>
- 769 Ellingson, S. W., Taylor, G. B., Craig, J., Hartman, J., Dowell, J., Wolfe, C. N., ...
770 Weiler, K. W. (2013). The lwa1 radio telescope. *IEEE Transactions on Anten-*
771 *nas and Propagation*, 61(5), 2540-2549. doi: 10.1109/TAP.2013.2242826
- 772 Hamlin, T., Krehbiel, P., Thomas, R., Rison, W., & Harlin, J. (2003). Electrical
773 structure and storm severity inferred by 3-d lightning mapping observations
774 during STEPS. In *Proc. 12th int. conf. on atmospheric electricity* (pp. 189–
775 192).
- 776 Hare, B., Scholten, O., Dwyer, J., Ebert, U., Nijdam, S., Bonardii, A., ... Winchen,
777 T. (2020). Radio emission reveals inner meter-scale structure of negative
778 lightning leader steps. *Phys. Rev. Lett.*, 124.
- 779 Hare, B. M., Scholten, O., Bonardi, A., Buitink, S., Corstanje, A., Ebert, U., ...
780 Winchen, T. (2018). Lofar lightning imaging: Mapping lightning with nanosec-
781 ond precision. *Journal of Geophysical Research: Atmospheres*, 123(5), 2861-
782 2876. Retrieved from [https://agupubs.onlinelibrary.wiley.com/doi/abs/](https://agupubs.onlinelibrary.wiley.com/doi/abs/10.1002/2017JD028132)
783 10.1002/2017JD028132 doi: 10.1002/2017JD028132

- 784 Hare, B. M., Scholten, O., Dwyer, J., Trinh, T., Buitink, S., Ter Veen, S., ... oth-
 785 ers (2019). Needle-like structures discovered on positively charged lightning
 786 branches. *Nature*, *568*(7752), 360–363.
- 787 Hare, B. M., Scholten, O., Dwyer, J. R., Strepka, C., Buitink, S., Corstanje, A., ...
 788 others (2020). Needle propagation and twinkling characteristics. *Earth and*
 789 *Space Science Open Archive ESSOAr*.
- 790 Hayenga, C. O. (1984). Characteristics of lightning vhf radiation near the time of
 791 return strokes. *Journal of Geophysical Research: Atmospheres*, *89*(D1), 1403-
 792 1410. Retrieved from [https://agupubs.onlinelibrary.wiley.com/doi/abs/
 793 10.1029/JD089iD01p01403](https://agupubs.onlinelibrary.wiley.com/doi/abs/10.1029/JD089iD01p01403) doi: 10.1029/JD089iD01p01403
- 794 Jensen, D., Sonnenfeld, R., Stanley, M., Edens, H., da Silva, C., & Krehbiel, P.
 795 (2021, February). *Supplementary Material for: Dart Leader and K Leader*
 796 *Velocity From Initiation Site to Termination Time-Resolved with 3D Interfer-*
 797 *ometry*. Zenodo. Retrieved from <https://doi.org/10.5281/zenodo.4561227>
 798 doi: 10.5281/zenodo.4561227
- 799 Jordan, D. M., Idone, V. P., Rakov, V. A., Uman, M. A., Beasley, W. H., & Ju-
 800 renka, H. (1992). Observed dart leader speed in natural and triggered light-
 801 ning. *Journal of Geophysical Research: Atmospheres*, *97*(D9), 9951-9957.
 802 Retrieved from [https://agupubs.onlinelibrary.wiley.com/doi/abs/
 803 10.1029/92JD00566](https://agupubs.onlinelibrary.wiley.com/doi/abs/10.1029/92JD00566) doi: 10.1029/92JD00566
- 804 Karunarathna, N., Marshall, T. C., Karunarathne, S., & Stolzenburg, M. (2017).
 805 Initiation locations of lightning flashes relative to radar reflectivity in four
 806 small florida thunderstorms. *Journal of Geophysical Research: Atmospheres*,
 807 *122*(12), 6565-6591. doi: 10.1002/2017JD026566
- 808 Kawasaki, Z., Mardiana, R., & Ushio, T. (2000). Broadband and narrowband rf in-
 809 terferometers for lightning observations. *Geophysical Research Letters*, *27*(19),
 810 3189-3192. Retrieved from [https://agupubs.onlinelibrary.wiley.com/
 811 doi/abs/10.1029/1999GL011058](https://agupubs.onlinelibrary.wiley.com/doi/abs/10.1029/1999GL011058) doi: 10.1029/1999GL011058
- 812 Kitagawa, N. (1957). On the mechanism of cloud flash and junction or final process
 813 in flash to ground. *Papers in Meteorology and Geophysics*, *7*(4), 415-424. doi:
 814 10.2467/mripapers1950.7.4.415
- 815 Krehbiel, P. R. (1986). The electrical structure of thunderstorms. In *The earth's*
 816 *electrical environment* (pp. 90–113). Washington, D.C.: National Academy
 817 Press.
- 818 Krehbiel, P. R., Rioussset, J. A., Pasko, V. P., Thomas, R. J., Rison, W., Stanley,
 819 M. A., & Edens, H. E. (2008). Upward electrical discharges from thunder-
 820 storms. *Nature Geoscience*, *1*(4), 233.
- 821 Liu, H., Qiu, S., & Dong, W. (2018). The three-dimensional locating of vhf broad-
 822 band lightning interferometers. *Atmosphere*, *9*(8), 317.
- 823 Loeb, L. B. (1966). The mechanisms of stepped and dart leaders in cloud-to-ground
 824 lightning strokes. *Journal of Geophysical Research (1896-1977)*, *71*(20), 4711-
 825 4721. Retrieved from [https://agupubs.onlinelibrary.wiley.com/doi/abs/
 826 10.1029/JZ071i020p04711](https://agupubs.onlinelibrary.wiley.com/doi/abs/10.1029/JZ071i020p04711) doi: 10.1029/JZ071i020p04711
- 827 Mardiana, R., Kawasaki, Z.-I., & Morimoto, T. (2002). Three-dimensional light-
 828 ning observations of cloud-to-ground flashes using broadband interferome-
 829 ters. *Journal of Atmospheric and Solar-Terrestrial Physics*, *64*(1), 91 - 103.
 830 Retrieved from [http://www.sciencedirect.com/science/article/pii/
 831 S1364682601000992](http://www.sciencedirect.com/science/article/pii/S1364682601000992) doi: [https://doi.org/10.1016/S1364-6826\(01\)00099-2](https://doi.org/10.1016/S1364-6826(01)00099-2)
- 832 Marshall, T. C., Stolzenburg, M., Maggio, C. R., Coleman, L. M., Krehbiel, P. R.,
 833 Hamlin, T., ... Rison, W. (2005). Observed electric fields associated
 834 with lightning initiation. *Geophysical Research Letters*, *32*(3). Retrieved
 835 from [https://agupubs.onlinelibrary.wiley.com/doi/abs/10.1029/
 836 2004GL021802](https://agupubs.onlinelibrary.wiley.com/doi/abs/10.1029/2004GL021802) doi: <https://doi.org/10.1029/2004GL021802>
- 837 Mazur, V. (2016). The physical concept of recoil leader formation. *Journal of Elec-*
 838 *trostatics*, *82*, 79–87.

- 839 Naidis, G. V. (2009, May). Positive and negative streamers in air: Velocity-diameter
840 relation. *Phys. Rev. E*, *79*, 057401. Retrieved from [https://link.aps.org/](https://link.aps.org/doi/10.1103/PhysRevE.79.057401)
841 [doi/10.1103/PhysRevE.79.057401](https://link.aps.org/doi/10.1103/PhysRevE.79.057401) doi: 10.1103/PhysRevE.79.057401
- 842 Oetzel, G. N., & Pierce, E. T. (1969). Vhf technique for locating light-
843 ning. *Radio Science*, *4*(3), 199-202. Retrieved from [https://agupubs](https://agupubs.onlinelibrary.wiley.com/doi/abs/10.1029/RS004i003p00199)
844 [.onlinelibrary.wiley.com/doi/abs/10.1029/RS004i003p00199](https://agupubs.onlinelibrary.wiley.com/doi/abs/10.1029/RS004i003p00199) doi:
845 10.1029/RS004i003p00199
- 846 Poehler, H., & Lennon, C. L. (1979). Lightning detection and ranging system lidar
847 system description and performance objectives. *NASA Technical Report*. Re-
848 trieved from <https://ntrs.nasa.gov/search.jsp?R=19790025501>
- 849 Proctor, D. E. (1971). A hyperbolic system for obtaining vhf radio pictures of
850 lightning. *Journal of Geophysical Research (1896-1977)*, *76*(6), 1478-1489.
851 Retrieved from [https://agupubs.onlinelibrary.wiley.com/doi/abs/](https://agupubs.onlinelibrary.wiley.com/doi/abs/10.1029/JC076i006p01478)
852 [10.1029/JC076i006p01478](https://agupubs.onlinelibrary.wiley.com/doi/abs/10.1029/JC076i006p01478) doi: 10.1029/JC076i006p01478
- 853 Rakov, V. A. (1998). Some inferences on the propagation mechanisms of dart leaders
854 and return strokes. *Journal of Geophysical Research: Atmospheres*, *103*(D2),
855 1879-1887. Retrieved from [https://agupubs.onlinelibrary.wiley.com/](https://agupubs.onlinelibrary.wiley.com/doi/abs/10.1029/97JD03116)
856 [doi/abs/10.1029/97JD03116](https://agupubs.onlinelibrary.wiley.com/doi/abs/10.1029/97JD03116) doi: 10.1029/97JD03116
- 857 Rakov, V. A., & Uman, M. A. (1990). Long continuing current in negative lightning
858 ground flashes. *J. Geophys. Res.*, *95*(D5), 5455-5470.
- 859 Rhodes, C. T., Shao, X. M., Krehbiel, P. R., Thomas, R. J., & Hayenga, C. O.
860 (1994). Observations of lightning phenomena using radio interferometry. *Jour-*
861 *nal of Geophysical Research: Atmospheres*, *99*(D6), 13059-13082. Retrieved
862 from [https://agupubs.onlinelibrary.wiley.com/doi/abs/10.1029/](https://agupubs.onlinelibrary.wiley.com/doi/abs/10.1029/94JD00318)
863 [94JD00318](https://agupubs.onlinelibrary.wiley.com/doi/abs/10.1029/94JD00318) doi: 10.1029/94JD00318
- 864 Rison, W., Thomas, R. J., Krehbiel, P. R., Hamlin, T., & Harlin, J. (1999). A
865 gps-based three-dimensional lightning mapping system: Initial observations
866 in central new mexico. *Geophysical Research Letters*, *26*(23), 3573-3576.
867 Retrieved from [https://agupubs.onlinelibrary.wiley.com/doi/abs/](https://agupubs.onlinelibrary.wiley.com/doi/abs/10.1029/1999GL010856)
868 [10.1029/1999GL010856](https://agupubs.onlinelibrary.wiley.com/doi/abs/10.1029/1999GL010856) doi: 10.1029/1999GL010856
- 869 Schonland, B. F. J., Malan, D. J., Collens, H., & Boys, C. V. (1935). Progres-
870 sive lightning ii. *Proceedings of the Royal Society of London. Series A -*
871 *Mathematical and Physical Sciences*, *152*(877), 595-625. Retrieved from
872 <https://royalsocietypublishing.org/doi/abs/10.1098/rspa.1935.0210>
873 doi: 10.1098/rspa.1935.0210
- 874 Shao, X. M., Holden, D. N., & Rhodes, C. T. (1996). Broad band radio interfer-
875 ometry for lightning observations. *Geophysical Research Letters*, *23*(15), 1917-
876 1920. Retrieved from [https://agupubs.onlinelibrary.wiley.com/doi/abs/](https://agupubs.onlinelibrary.wiley.com/doi/abs/10.1029/96GL00474)
877 [10.1029/96GL00474](https://agupubs.onlinelibrary.wiley.com/doi/abs/10.1029/96GL00474) doi: 10.1029/96GL00474
- 878 Shao, X. M., & Krehbiel, P. R. (1996). The spatial and temporal development of in-
879 tracloud lightning. *Journal of Geophysical Research: Atmospheres*, *101*(D21),
880 26641-26668. Retrieved from [https://agupubs.onlinelibrary.wiley.com/](https://agupubs.onlinelibrary.wiley.com/doi/abs/10.1029/96JD01803)
881 [doi/abs/10.1029/96JD01803](https://agupubs.onlinelibrary.wiley.com/doi/abs/10.1029/96JD01803) doi: 10.1029/96JD01803
- 882 Shao, X. M., Krehbiel, P. R., Thomas, R. J., & Rison, W. (1995). Radio interfero-
883 metric observations of cloud-to-ground lightning phenomena in florida. *Journal*
884 *of Geophysical Research: Atmospheres*, *100*(D2), 2749-2783. Retrieved from
885 <https://agupubs.onlinelibrary.wiley.com/doi/abs/10.1029/94JD01943>
886 doi: 10.1029/94JD01943
- 887 Stanley, M., Krehbiel, P. R., Fan, X., Edens, H. E., Rodeheffer, D., Rison, W., ...
888 Rubinstein, M. (2020). Initial results from a 2nd-generation broadband
889 vhf interferometer imaging system. In *Agu fall meeting abstracts* (Vol. 2020,
890 p. AE006-12).
- 891 Stock, M. (2014). *Broadband interferometry of lightning*. New Mexico Institute of
892 Mining and Technology.
- 893 Stock, M., Akita, M., Krehbiel, P., Rison, W., Edens, H., Kawasaki, Z., & Stanley,

- 894 M. (2014). Continuous broadband digital interferometry of lightning using
895 a generalized cross-correlation algorithm. *Journal of Geophysical Research:
896 Atmospheres*, 119(6), 3134–3165.
- 897 Thomas, R. J., Krehbiel, P. R., Rison, W., Hamlin, T., Boccippio, D. J., Goodman,
898 S. J., & Christian, H. J. (2000). Comparison of ground-based 3-dimensional
899 lightning mapping observations with satellite-based LIS observations in Okla-
900 homa. *Geophys. Res. Lett.*, 27(12), 1703–1706.
- 901 Thomas, R. J., Krehbiel, P. R., Rison, W., Hunyady, S. J., Winn, W. P., Hamlin,
902 T., & Harlin, J. (2004). Accuracy of the lightning mapping array. *Journal
903 of Geophysical Research: Atmospheres*, 109(D14). Retrieved from [https://
904 agupubs.onlinelibrary.wiley.com/doi/abs/10.1029/2004JD004549](https://agupubs.onlinelibrary.wiley.com/doi/abs/10.1029/2004JD004549) doi:
905 10.1029/2004JD004549
- 906 Thyer, N. (1962). Double theodolite pibal evaluation by computer. *Journal of ap-
907 plied meteorology*, 1(1), 66–68.
- 908 Warwick, J. W., Hayenga, C. O., & Brosnahan, J. W. (1979). Interferometric direc-
909 tions of lightning sources at 34 mhz. *Journal of Geophysical Research: Oceans*,
910 84(C5), 2457–2468. Retrieved from [https://agupubs.onlinelibrary.wiley
911 .com/doi/abs/10.1029/JC084iC05p02457](https://agupubs.onlinelibrary.wiley.com/doi/abs/10.1029/JC084iC05p02457) doi: 10.1029/JC084iC05p02457
- 912 Williams, E. R. (1989). The tripole structure of thunderstorms. *Journal of Geophys-
913 ical Research: Atmospheres*, 94(D11), 13151–13167. Retrieved from [https://
914 agupubs.onlinelibrary.wiley.com/doi/abs/10.1029/JD094iD11p13151](https://agupubs.onlinelibrary.wiley.com/doi/abs/10.1029/JD094iD11p13151)
915 doi: 10.1029/JD094iD11p13151
- 916 Winn, W. P. (1965). A laboratory analog to the dart leader and return stroke of
917 lightning. *Journal of Geophysical Research (1896-1977)*, 70(14), 3265–3270.
918 Retrieved from [https://agupubs.onlinelibrary.wiley.com/doi/abs/
919 10.1029/JZ070i014p03265](https://agupubs.onlinelibrary.wiley.com/doi/abs/10.1029/JZ070i014p03265) doi: 10.1029/JZ070i014p03265
- 920 Winn, W. P., Aulich, G. D., Hunyady, S. J., Eack, K. B., Edens, H. E., Kre-
921 hbiel, P. R., ... Sonnenfeld, R. G. (2011). Lightning leader stepping, k
922 changes, and other observations near an intracloud flash. *Journal of Geo-
923 physical Research: Atmospheres*, 116(D23). Retrieved from [https://
924 agupubs.onlinelibrary.wiley.com/doi/abs/10.1029/2011JD015998](https://agupubs.onlinelibrary.wiley.com/doi/abs/10.1029/2011JD015998) doi:
925 10.1029/2011JD015998
- 926 Wu, T., Wang, D., & Takagi, N. (2018). Lightning mapping with an array of
927 fast antennas. *Geophysical Research Letters*, 45(8), 3698–3705. Retrieved
928 from [https://agupubs.onlinelibrary.wiley.com/doi/abs/10.1002/
929 2018GL077628](https://agupubs.onlinelibrary.wiley.com/doi/abs/10.1002/2018GL077628) doi: 10.1002/2018GL077628